ISPRS Journal of Photogrammetry and Remote Sensing 94 (2014) 194–212

Contents lists available at ScienceDirect

ISPRS Journal of Photogrammetry and Remote Sensing

journal homepage: www.elsevier.com/locate/isprsjprs

Derivation of an urban materials spectral library through emittance and reflectance spectroscopy

Simone Kotthaus [a,b,*], Thomas E.L. Smith [b], Martin J. Wooster [b,c], C.S.B. Grimmond [a,b]

[a] Department of Meteorology, University of Reading, Earley Gate, PO Box 243, Reading RG6 6BB, UK
[b] King's College London, Department of Geography, The Strand, London WC2R 2LS, UK
[c] NERC National Centre for Earth Observation, UK

ARTICLE INFO

Article history:
Received 17 February 2014
Received in revised form 15 April 2014
Accepted 5 May 2014
Available online 9 June 2014

Keywords:
Spectral library
Impervious materials
FTIR spectroscopy
Reflectance
Emissivity

ABSTRACT

Recent advances in thermal infrared remote sensing include the increased availability of airborne hyperspectral imagers (such as the Hyperspectral Thermal Emission Spectrometer, HyTES, or the Telops HyperCam and the Specim aisaOWL), and it is planned that an increased number spectral bands in the long-wave infrared (LWIR) region will soon be measured from space at reasonably high spatial resolution (by imagers such as HyspIRI). Detailed LWIR emissivity spectra are required to best interpret the observations from such systems. This includes the highly heterogeneous urban environment, whose construction materials are not yet particularly well represented in spectral libraries. Here, we present a new online spectral library of urban construction materials including LWIR emissivity spectra of 74 samples of impervious surfaces derived using measurements made by a portable Fourier Transform InfraRed (FTIR) spectrometer. FTIR emissivity measurements need to be carefully made, else they are prone to a series of errors relating to instrumental setup and radiometric calibration, which here relies on external blackbody sources. The performance of the laboratory-based emissivity measurement approach applied here, that in future can also be deployed in the field (e.g. to examine urban materials *in situ*), is evaluated herein. Our spectral library also contains matching short-wave (VIS–SWIR) reflectance spectra observed for each urban sample. This allows us to examine which characteristic (LWIR and) spectral signatures may in future best allow for the identification and discrimination of the various urban construction materials, that often overlap with respect to their chemical/mineralogical constituents. Hyperspectral or even strongly multi-spectral LWIR information appears especially useful, given that many urban materials are composed of minerals exhibiting notable reststrahlen/absorption effects in this spectral region. The final spectra and interpretations are included in the London Urban Micromet data Archive (LUMA; http://LondonClimate.info/LUMA/SLUM.html).

1. Introduction

Recent advances in thermal infrared remote sensing (Kuenzer and Dech, 2013) include a new generation of space- and airborne hyperspectral thermal sensors such as HyTES and HyspIRI (Abrams and Hook, 2013; Hook et al., 2013), and progress in ground-based techniques (methods and instruments) used both in the field and laboratory (Hecker et al., 2013). Spectrally detailed information across the long-wave infrared (LWIR) atmospheric window offers great potential to aid with a series of challenges of earth observation: it provides new insights and data for the development and application of algorithms aiming at the separation of surface temperature and surface emissivity effects in LWIR spectra and imagery (e.g. Peres et al., 2008) and for the subsequent use of these types of information in e.g. energy balance models (e.g. Xu et al., 2008), and also potentially aids the improved characterisation and classification of surface properties, material type, and surface change through the addition of LWIR information to that in the more commonly exploited VIS-to-SWIR solar reflected spectral regions (e.g. French et al., 2008).

However, current LWIR spectral library information such as that in the widely used ASTER (Advanced Spaceborne Thermal Emission and Reflection Radiometer) spectral library (Baldridge et al., 2009) does not adequately cover the immense diversity of urban materials

* Corresponding author at: Department of Meteorology, University of Reading, Earley Gate, PO Box 243, Reading RG6 6BB, UK. Tel.: +44 (0)118 378 5419; fax: +44 (0)118 378 8905.
E-mail address: s.kotthaus@reading.ac.uk (S. Kotthaus).

http://dx.doi.org/10.1016/j.isprsjprs.2014.05.005
0924-2716/

(Heiden et al., 2007), even though this will be crucial for the interpretation of hyperspectral remote sensing data gathered in such areas in the future. Urban surface properties have important implications for human health, sustainable design and climate change adaptation and hence present fundamental modelling parameters for related studies (Yang, 2011). In particular, the radiative response of impervious urban materials determines the radiation balance of incoming and outgoing long- and short-wave fluxes, and thereby urban climate conditions. Its significance recently received global media attention when solar radiation reflected by the curved façade[1] of a new skyscraper in the City of London was sometimes intense enough to create surface temperatures sufficient to melt particular plastic parts of nearby parked cars (Guardian, 2013). Spectral information covering the LWIR can also help to support surface temperature retrieval algorithms relevant to research concerned with urban climate and air quality. Relations between short-wave albedo and long-wave emissivity/surface temperature (Small, 2006) are of particular interest for urban climate studies concerned with human thermal comfort (Matzarakis et al., 2010) and/or building energy demand (Yaghoobian and Kleissl, 2012). The surface kinetic temperature (or even the surface brightness temperature directly, i.e. ignoring effects of emissivity) is often used to study the surface urban heat island phenomenon (Voogt and Oke, 2003), to model surface energy exchanges (Voogt and Grimmond, 2000; Xu et al., 2008), and to evaluate and improve urban canopy models (Kusaka et al., 2001).

This paper aims to support such work by developing a new urban materials spectral library covering both the LWIR and VIS–SWIR atmospheric windows, and by elucidating the methods and uncertainties inherent in the production of such a database using, respectively, Fourier Transform InfraRed (FTIR) and grating-based spectrometry. Some background information is provided to underline the motivation of this study (Section 2). Then, the applied spectroscopy methods are introduced (Section 3), providing details on radiometric calibration, background correction and the separation of emissivity and temperature. Investigations of the thermal properties of reference radiation sources (that provide the basis for the radiometric calibration) permit uncertainties arising from the methodology to be quantified. A framework for laboratory-based FTIR emissivity observations is developed (similarly applicable outdoors) and spectra of the different material-classes are analysed (Section 4). Finally, uncertainties of the FTIR spectroscopy observations are summarised and implications of the results for remote sensing of impervious urban materials are considered (Section 5).

2. Motivation

Current spectral libraries provide information on a wide variety of materials (e.g. MODIS spectral library, Moderate Resolution Imaging Spectroradiometer, Wan et al., 1994; US Geological Survey, USGS, Clark et al., 2007; ASTER, Baldridge et al., 2009), however, their coverage of impervious urban materials remains limited, especially in the LWIR spectral region (e.g. see Table 1).

Urban spectral libraries have been developed from airborne and/or ground truth observations for example in: Tel-Aviv, Israel (Ben-Dor et al., 2001 using library spectra of Price, 1995), Potsdam and Dresden, Germany (Heiden et al., 2001; Roessner et al., 2001; Heiden et al., 2007), Bonn, Germany (Franke et al., 2009) and Santa Barbara, USA (Herold et al., 2004; Herold, 2007), with increasing interest in the LWIR spectral response of anthropogenic materials. Only a few studies include *in situ* measurements of the same surfaces covering short and long wavelengths (e.g. Kerekes et al., 2008).

[1] Note: this façade was glass which is not a focus of this study.

Cities are very complex spatially, given their three-dimensional structure and immense heterogeneity. But also temporally conditions are changing at fast rates compared to many more 'natural' environments, due to human movements, re-construction (new developments replacing old structures) or technological advances in manufacturing techniques (making new construction materials available). The latter may be used to reduce costs or to yield novel architectural benefits (e.g. flexibility of PVC), but increasingly the environmental aspects of materials and surfaces are being considered in the context of climate change mitigation. Highly reflecting materials are deployed to reduce absorption of solar energy at the surface, which can help to cool urban areas (Akbari et al., 2009). Furthermore, with the need to reduce life-cycle carbon emissions (e.g. DCLG, 2013) there is demand to replace materials (e.g. demand for carbon–neutral cement, Damtoft et al., 2008). Knowledge about chemical compositions and radiative properties of both novel and older construction materials is required to ensure that their dynamic impacts are incorporated into our understanding of the ever-changing urban environment. Applications in a research context range from the characterisation of sites where atmospheric quantities are measured and modelled *in situ* to improved interpretation of airborne or satellite remote sensing data.

As many materials have distinct spectral absorption features in the visible to short-wave infrared (VIS–SWIR) region of the electromagnetic spectrum, multi- or hyper-spectral information across the these wavelengths is applicable to a variety of environmental research questions (e.g. Clark, 1999). Amongst others, they provide a basis for the land cover classification of natural materials, such as soil types (Rossel et al., 2006), vegetation (Adam et al., 2010), and also anthropogenic materials (Townshend et al., 1991). This requires some *a priori* knowledge of the materials' spectral characteristics (Heiden et al., 2001), usually obtained from "ground truth" field spectroscopy, often carried out simultaneously with air-/space-borne data acquisition, and/or from spectral libraries. Urban applications of such classifications (Weng, 2012) cover a wide range of purposes; such as mapping of urbanisation (Deng et al., 2009), identification of impervious surface cover for the quantification of flood risk (Schueler, 1994), assessment of concrete quality (Brook and Ben-Dor, 2011), and evaluation of road network conditions (Herold et al., 2003; Pascucci et al., 2008).

Some materials however, pose a challenge to land cover classification algorithms based on VIS–SWIR information because they lack distinct features in this spectral region. Roberts et al. (2012) suggest that urban land cover classification (e.g. differentiation between bare soil and asphalt) could be significantly improved by including hyperspectral LWIR data, emphasising the great potential of a comprehensive LWIR spectral library. This is because many materials are featureless at shorter wavelengths (e.g. mineral composites, Cloutis et al., 2008), but reveal clear absorption and reststrahlen bands in the LWIR region. The *reststrahlen* (German, 'residual rays') effect describes reflection of radiation in a certain absorption band due to changes of the refractive index within the medium. In combination with absorption features, the related wavebands ('reststrahlen bands') allow conclusions to be drawn about the material's molecular structure.

In addition to the benefits to land cover classification, spectral LWIR emissivity is valuable because it relates outgoing radiance, or a body's 'brightness temperature', to its actual surface kinetic temperature (Gillespie et al., 1998), often termed the land surface temperature (LST; Tomlinson et al., 2011). All LWIR remote sensing approaches aimed at surface kinetic temperature/LST estimation require a method to partition the measured radiance into its contributions from the kinetic temperature of the surface and its emissivity. Several such temperature–emissivity–separation (TES) algorithms have been developed (e.g. Gillespie et al., 1998; Dash

Table 1
Spectral libraries of anthropogenic materials (by year of publication). Specifications given (i.e. spectral range, instrumentation and data acquisition) relevant to the spectral information used in this study. More spectra might be available in respective libraries that cover different wavelengths and/or are measured with other devices.

Reference	Study area	Materials	Spectral range [nm]	Instrumentation	Data acquisition
Wan et al. (1994) *MODIS UCSB emissivity library	Various locations, USA	Building, roofing, pavement, road	3300–14500	MIDAC M2510-C FTIR	Laboratory
Ben-Dor et al. (2001)	Tel-Aviv, Israel	Building, roofing, pavement, road, sports infrastructure	430–940	CASI & ASD FieldSpec3	Airborne & *in situ*
Heiden et al. (2001, 2007)	Dresden & Potsdam, Germany	Building, roofing, pavement, road, partially impervious	400–2500	HyMap & ASD Fieldspec3	Airborne & *in situ*
Herold et al. (2004) *Santa Barbara (SB) spectral library	Santa Barbara, CA, USA	Building, roofing, pavement, road, sports infrastructure	350–2400	ASD FieldSpec3	*In situ*
Baldridge et al. (2009) *ASTER spectral library	Various locations, USA	Building, roofing, pavement, road, paint	400–15400	Perkin–Elmer Lambda 900 UV/VIS/NIR, Perknic & Nicolet 520FT-IR	Laboratory
Clark et al. (2007) *USGS spectral library	Various locations, USA	Building, roofing, pavement, road, plastic	400–3000	Beckman 5270 & ASD FieldSpec3	Laboratory
Nasarudin and Shafri (2011)	University campus, Malaysia	Roofing, road	350–2500	ASD FieldSpec3	*In situ*

* Data are freely available on the web.

et al., 2002), and their methods depend somewhat on the sensor specifications (e.g. number of separate LWIR spectral channels available). The very limited work on urban-specific materials (Sobrino et al., 2012) suggests that such methods can provide appropriate emissivity estimates in cities (e.g. Xu et al., 2008; Sobrino et al., 2012). However, emissivity of some complex anthropogenic materials (e.g. metals) remains difficult to characterise (Sobrino et al., 2012). A more comprehensive library of urban building materials covering both the VIS–SWIR and LWIR regions could provide a foundation for these continually developing TES methodologies to be more applicable in city environments.

We use FTIR field spectroscopy to measure LWIR spectra. FTIR spectroscopy is a commonly used technique to measure spectral thermal radiance with portable instrumentation (Griffiths, 1983; Korb et al., 1996). Widely applied to observe absorption spectra from gases (e.g. Wooster et al., 2011), this technique is also used to quantify surface emissivity (absorbance) of solid surfaces (Breen et al., 2008), commonly by direct measurements of the sample's thermal emitted radiance (e.g. Ruff et al., 1997; Christensen et al., 2000; Kerekes et al., 2008). To make usable observations that make surface emissivity extraction possible from the data, and to generally improve the signal-to-noise ratio of the measurements, the samples' emitted LWIR radiance signal needs to significantly exceed that coming from the ambient background (e.g. the sky outdoors, or indoor the ceiling/walls of the surrounding room) (Horton et al., 1998). Indoors this is normally done by heating the sample prior to measurement. Radiometric calibration of the observed energy spectrum commonly relies on further supplementary measurements of radiation sources of known temperature and emissivity, the latter introducing further measurement uncertainty (Lindermeir et al., 1992) due to imprecise knowledge of e.g. the calibration source's surface homogeneity.

The objectives of this study relate to both the methodology and the observed results. Two spectroscopy methods were used to derive short-wave (VIS–SWIR) reflectance and long-wave (LWIR) emissivity measures for samples of impervious materials found across a major city, London, UK. Given that portable FTIR spectrometers now enable emissivity observations to be performed in standard laboratories or even in the field (rather than being confined to highly specialised laboratories), this methodology is evaluated. Measurement uncertainties are quantified specifically for a setting with moderate temperatures (40–70 °C) chosen for the collection of emissivity spectra in this study. The observed VIS–SWIR reflectance and LWIR emissivity spectra are interpreted to assess the variability of the spectral characteristics of building materials studied.

3. Methods

As with most spectral libraries (e.g. USGS and ASTER), the measurements made here were conducted under controlled laboratory conditions. Certain types of samples however may require a spectrometer to be used in the field, even though no information can be obtained in the spectral regions where atmospheric water vapour absorption is high (Joseph, 2005). In such cases, the spectroscopy methods and equipment used here could also be applied outdoors (see Appendix A).

The wavelength (λ) dependence of infrared radiance L_λ emitted by an ideal emitter (a perfect blackbody, *BB*) at temperature T follows Planck's radiation law (Planck, 1901):

$$L_\lambda(T)_{BB} = \frac{2h}{\lambda c^2}\frac{1}{e^{\frac{h}{\lambda kT}}-1} \quad (1)$$

with the Planck constant h, speed of light c and Boltzmann constant k. Spectral emissivity represents the fraction of the spectral radiance R_λ emitted by an object of kinetic temperature T relative to that emitted by a perfect blackbody at the same kinetic temprature L_λ:

$$\varepsilon_\lambda = \frac{R_\lambda(T)}{L_\lambda(T)_{BB}} \quad (2)$$

Hence, measurements of the sample's thermal emitted radiance spectra can be used to derive spectral emissivity information (e.g. Ruff et al., 1997; Christensen et al., 2000; Kerekes et al., 2008). Short-wave reflectance spectra α_λ were derived as the fraction of incoming radiance reflected by the target in the VIS–SWIR spectral region.

Here, LWIR target spectral radiance data are gathered using an FTIR spectrometer that records an energy spectrum in raw digital numbers (DNs). The radiometric calibration of the latter into units of radiance requires auxiliary information, here obtained via two blackbody sources at different temperatures that are sampled along with the targets. The target-leaving radiance observed with the spectrometer is composed of an emitted fraction (related to the target's kinetic temperature and emissivity) and the reflected incoming radiance originating from the background (i.e. laboratory's walls and ceiling; or the sky if outdoors). This component is measured by observing the radiance spectra from a reference target of low emissivity and thus high reflectivity (a gold reference panel). To improve the signal-to-noise ratio, the radiance emitted by the target was kept high relative to the incoming reflected thermal radiance, essentially by heating the samples well above room temperature.

3.1. Measurement setup

3.1.1. Short-wave reflectance spectroscopy

Laboratory observations of VIS–SWIR reflectance spectra of various materials were conducted with an HR-1024 field spectroradiometer (SVC, *Spectra Vista Corporation*, Poughkeepsie, NY, USA). The instrument has three diffraction grating spectrometers: one silicon (512 discrete detectors) and two indium gallium arsenide (InGaAs; 256 discrete detectors each) diode arrays. The 1024 spectral bands cover the measurement range of 350–2500 nm, with resolutions of $\leqslant$3.5 nm (350–1000 nm), $\leqslant$9.5 nm (1000–1850 nm), and $\leqslant$6.5 nm (1850–2500 nm). Calibration into spectral radiance units is performed by the SVC HR-1024 PC data acquisition software. Radiance from the target and the reference panel, respectively, were stored along with the relative reflectance derived. As fore-optics a 4° field of view (FOV) lens was applied resulting in an instantaneous FOV of ~25 mm at a 350 mm distance between lens and target.

To ensure strong, uniform illumination two 300 W Videolight 6 (*Kaiser Fototechnik*, Buchen, Germany) lamps were used. The SVC HR-1024 sensor detects a cone of upwelling radiation, so that the setup was between bi-conical and hemispherical–conical. Irradiance was measured by sampling a surface of known high reflectivity that approximates a completely Lambertian surface. Here, a "white" Spectralon reflectance panel with a VIS–SWIR broadband albedo of 0.98 (serial number 4240A, calibrated by NERC FSF, National Environmental Research Council Field Spectroscopy Facility, on 21/03/2010) was used. Its reflectance spectra were collected at the same nadir viewing geometry (i.e. 0° zenith angle) as the target.

Absolute spectral reflectance α_λ was calculated by dividing the target radiance $R_{\lambda T}$ by the reference panel radiance $R_{\lambda R}$, incorporating the non-unity spectral reflectance of the reference panel p_λ (NERC FSF calibration): $\alpha_\lambda = (R_{\lambda T}/R_{\lambda R}) \times p_\lambda$. All targets were sampled ten times in total, observing two different areas of the target's surface (5 samples each) to get a first order estimate of the material's potential spatial surface inhomogeneity. The reference panel was measured once preceding the target measurements.

It should be noted that the VIS–SWIR reflectance spectra do not represent actual hemispherical reflectance measures. Even though two light sources were used to illuminate the sample, which gives a more homogeneous field of irradiance than a single source, the conically observed reflected radiation was measured only at a single fixed angle. Given most of the observed materials cannot be assumed to be fully Lambertian, directional reflectance variations can be expected which are not captured by the data collected here. To completely characterise the samples' BRDF (bi-directional reflectance distribution function) a significantly more complex measurement setup would be required. The absorption signatures discussed (the main focus of this work) are less influenced by these directional variations because their locations correspond to the material's molecular structure. Their depth, however, may be slightly altered when viewed from different angles. Many remotely sensed short-wave reflectance estimates have these directional limitations, so integrated values from such approaches should be used with care. This becomes especially critical for materials with highly specular characteristics (such as glass), which are commonly found in urban areas. Still, useful information about the overall albedo (here approximated as the spectrally integrated bi-directional reflectance, Appendix C) of the various materials studied can be gained from the bi-directional spectra.

3.1.2. Long-wave emission spectroscopy

Long-wave target radiance was measured with a M2000 Fourier Transform InfraRed spectrometer (FTIR, *MIDAC*, Westfield, MA, USA), across a spectral range of 650–5000 cm^{-1} (2.0–15.4 μm) at a spectral resolution of 2 cm^{-1}. Data analysis focused on the 8.0–14.0 μm LWIR region, as the signal-to-noise performance of the FTIR significantly declines at shorter wavelengths when observing objects at temperatures <~100 °C as is the case here. Since the thermal emittance signal of Earth surface materials at ambient temperatures peak in the LWIR region, this is the spectral region most important for surface emissivity investigations related to kinetic temperature determination. Further, it bears crucial information about the long-wave response of impervious construction materials given the presence of the many reststrahlen bands of abundant minerals (Clark, 1999).

Each spectral measurement consisted of 16 consecutively sampled spectra, and each target was measured ten times after single measurements of two IR-2100 Blackbody Systems (*Infrared Systems Development*, Winter Park, FL, USA) and the InfraGold reference panel (*Labsphere*, North Sutton, NH, USA), respectively. This strategy was chosen because the combination of ten samples improves the signal-to-noise ratio while allowing a set of measurements to be collected in a relatively short time period (~2 min). This is important as incoming radiance and instrument response are assumed stable throughout this time. The latter assumption is tested (Section 4.1.3).

The flat plate blackbody sources have an aperture of 63.5 mm × 63.5 mm and a spectrally flat surface emissivity of 0.96. The gold standard has a mean spectral emissivity of 0.05 across the LWIR region, and the manufacturer specified spectral emissivity curve (50 cm^{-1} spectral resolution) was resampled to match the 2 cm^{-1} spectral resolution of the FTIR observations. The blackbodies, gold reference panel and targets were swapped manually and placed vertically in front of the spectrometer at a distance of about 100 mm, at which point the spectrometer's FOV subtends a diameter of about 30 mm (Chris MacLellan, NERC FSF, personal communication). In order to improve stability of the thermal conditions, the FTIR was switched on an hour prior to the measurement commencement, allowing it to reach its operation temperature. Given that the measurements were performed in the laboratory, the samples were heated to moderate temperatures of 50–60 °C. The two adjustable blackbodies were set to temperatures of 40–45 °C and 70 °C respectively, in order to bracket the target temperature.

Auxiliary information on the performance of the blackbody sources were collected with a TESTO 875-1 thermal imaging camera (*TESTO*, Alton, Hampshire, UK) with a resolution of 160 × 120 and a spectral range of 8–14 μm. The IR camera was calibrated against a radiation standard, a cavity IR-563/301 Blackbody System (*Infrared Systems Development*) with a small aperture (~20 mm) and an emissivity of >0.99, over a temperature range of 50–100 °C. An independent, extended area (304 × 304 mm) blackbody source, an IR-140/301 Blackbody System (*Infrared Systems Development*) with an emissivity of 0.96, was also used in this assessment.

3.2. Data processing

Data processing used R (version 15.2, R Core Team, 2005) scripts, developed based on NERC FSF guidelines and the FSF post processing MATLAB toolbox (Robinson and Mac Arthur, 2012). The HR-1024 measurement software stores VIS–SWIR radiance spectra observed from the reference panel and target, respectively, and the derived relative reflectance with the meta information in text files (*.sig; SVC). The FTIR data collection software (AutoQuant Pro, *MIDAC*) creates a binary file format (*.sb) that was converted to text files (*.csv) using an IDL (version 8.2.1, EXELIS Visual Information Solutions) script. Wavelengths in the VIS–SWIR (LWIR) are given in units of nm (μm).

Albedo, the broadband estimate of reflectance covering the region 300–2500 nm, is weighted by a standard terrestrial solar spectrum (*ASTM G173-03* global solar spectrum, NREL, 2000) and integrated spectrally. Broadband emissivity is integrated over the

wavelength region of 8–14 μm and normalised by the Planck radiance spectrum (Eq. (1)) calculated at 290 K, a typical value for urban surface temperatures in mid-latitudes.

3.2.1. Short-wave reflectance

The measurement ranges of the silicon detector array and the first InGaAs detector array overlap slightly in the transition region of 960–1005 nm. Although the SVC software allows removal of the overlap to store a continuous spectrum, the complete measurements were stored to avoid uncontrolled loss of information (NERC FSF personal communication). During post processing, overlapping data were interpolated by fitting a cubic spline through data from the long-wave end of the first and the short-wave end of the second detector array. This created a combined spectrum using the wavelengths of the latter to 980 nm. Removing this overlapping region reduced the number of available bands from 1024 to 988. Following calculation of the absolute reflectance (α_λ), smoothing via the Savitzky–Golay filter (Savitzky and Golay, 1964) was used with a frame size of 31 (Robinson and Mac Arthur, 2012). The final short-wave reflectance spectra for each target were obtained by averaging the respective samples.

3.2.2. Long-wave emissivity

3.2.2.1. Radiometric calibration. As internal parts of the infrared spectrometer (e.g. mirrors, lenses) interact with the incoming radiation, they also alter the recorded energy spectrum. These effects can be described by an instrument specific calibration. Radiation entering the instrument R_λ is retrieved from the detected energy spectrum E_λ (raw digital numbers, DNs) by accounting for the instrument response of the spectrometer G_λ, hereafter referred to as *gain*, and the instrument's self-emission S_λ, i.e. the spectral radiance originating from inside the spectrometer:

$$R_\lambda = S_\lambda + G_\lambda \cdot E_\lambda \tag{3}$$

For many techniques, the gain is quite stable and can be calculated theoretically or measured under specialised laboratory conditions. When observing thermal radiance, however, instrument-internal conditions themselves vary with the observed quantity so that calibration needs to be performed near simultaneously with the measurement itself. To account for the complex effects of the instrument components several instantaneous calibration techniques have been developed for thermal remote sensing applications (e.g. Revercomb et al., 1988; Lindermeir et al., 1992; Hook and Kahle, 1996; Ruff et al., 1997). These usually involve reference observations of one or multiple blackbody systems (i.e. sources of 'known' radiance) simultaneously or in turn with the sampling of the target.

A commonly used approach is the 2BB-method (e.g. Hook and Kahle, 1996; Korb et al., 1996), where two blackbodies of known temperature (T_{BB1}, T_{BB2}) are measured along with the target. Given their emitted radiance R_λ can be described by Planck's law, when incorporating their non-unitary emissivity, coefficients for radiometric calibration can be obtained from their radiance:

$$\begin{aligned} R_\lambda(T_{BB1}) &= S_\lambda + G_\lambda \cdot E_\lambda(T_{BB1}) \\ R_\lambda(T_{BB2}) &= S_\lambda + G_\lambda \cdot E_\lambda(T_{BB2}) \end{aligned} \tag{4}$$

Under the assumption of a linear radiometric response with incoming spectral radiance, these equations can be combined to calculate instrument self-emission and gain:

$$S_\lambda = \frac{R_\lambda(T_{BB1})E_\lambda(T_{BB2}) - R_\lambda(T_{BB2})E_\lambda(T_{BB1})}{E_\lambda(T_{BB2}) - E_\lambda(T_{BB1})} \tag{5a}$$

$$G_\lambda = \frac{R_\lambda(T_{BB2}) - R_\lambda(T_{BB1})}{E_\lambda(T_{BB2}) - E_\lambda(T_{BB1})} \tag{5b}$$

Based on these spectrally varying coefficients, the detected energy spectrum from observing the target $E_\lambda(T_{target})$ can be calibrated to the target's radiance (Eq. (3)). Measurements of the blackbodies should be performed directly before/after sampling the target to minimise potential effects of instrument drift (Salvaggio and Miller, 2001) and changes in background conditions. The accuracy to which we know the kinetic temperatures of the reference blackbody systems (T_{BB1}, T_{BB2}) adds uncertainty to the calibrated target radiance, thus emphasising the need for high quality equipment and careful operation (e.g. enough time for the BB systems to stabilise at the set temperature). Even though there are approaches to circumvent this limitation (e.g. using three BBs to gain additional information, Lindermeir et al., 1992), they are not yet well established and the 2-BB method remains the most commonly used calibration method (e.g. Hook and Kahle, 1996; Bassani et al., 2007).

3.2.2.2. 'Background' correction. The 'background' correction addresses the impact of incoming radiation from the surroundings (e.g. cool outside 'sky', or warmer lab walls and ceilings) and the atmospheric paths through which the radiation travels. Radiance leaving a target of temperature T_{target} is composed of radiance emitted by a blackbody at the same temperature $L_\lambda(T_{target})_{BB}$, which is expressed by the Planck function (Eq. (1)), multiplied by the target's emissivity ε_λ, the path thermal radiance of the air between the target and the sensor $R_\lambda(T_{air})_p$ and the down-welling radiance emitted from the background $R_{\lambda d}$, the latter reflected by the target (assuming it has a non-unitary emissivity). Taking into account the transmissivity of the atmosphere between the emitter and the measurement device, τ_λ, the relation can be expressed (Ottle and Stoll, 1993):

$$R_\lambda(T_{target}) = \tau_\lambda|\varepsilon_\lambda L_\lambda(T_{target})_{BB} + (1-\varepsilon_\lambda)R_{\lambda d}| + R_\lambda(T_{air})_p \tag{6}$$

Given the very short distance between the target and the sensor for the spectroscopic observations in this study, which are made in the 8–14 μm atmospheric window, atmospheric emission along the path is neglected ($R_\lambda(T_{air})_p = 0$) and perfect atmospheric transmissivity ($\tau_\lambda = 1$) is assumed. Eq. (6) then simplifies to:

$$R_\lambda(T_{target}) = |\varepsilon_\lambda L_\lambda(T_{target})_{BB} + (1-\varepsilon_\lambda)R_{\lambda d}| \tag{7}$$

i.e. the radiance leaving the target is composed of the radiance emitted by the latter, plus the fraction $(1-\varepsilon_\lambda)$ of down-welling radiance reflected. Measuring a target with known spectral emissivity and diffuse reflectance characteristics, here the gold reference panel with spectral emissivity $(\varepsilon_\lambda)_{gold}$, allows this equation to provide an estimate of the down-welling spectral radiance $R_{\lambda d}$, assuming the latter is isotropic. $R_{\lambda d}$ is the difference between the calibrated radiance observed from the gold reference $R_\lambda(T_{gold})$ and the Planck radiance (Eq. (1)) of a BB at the temperature of the reference panel $L_\lambda(T_{gold})_{BB}$, taking into account the spectral emissivity of the gold plate:

$$R_{\lambda d} = \frac{R_\lambda(T_{gold}) - (\varepsilon_\lambda)_{gold}L_\lambda(T_{target})_{BB}}{1-(\varepsilon_\lambda)_{gold}} \tag{8}$$

Assuming background conditions remain constant throughout the measurement, this down-welling radiance is then used within a re-arrangement of Eq. (7) to calculate the target's absolute emissivity spectrum:

$$\varepsilon_\lambda = \frac{R_\lambda(T_{target}) - R_{\lambda d}}{L_\lambda(T_{target})_{BB} - R_{\lambda d}} \tag{9}$$

3.2.2.3. Separation of emissivity and temperature. The target temperature T_{target} is required (Eq. (9)) to calculate the respective Planck radiance $L_\lambda(T_{target})_{BB}$. Given the difficulty in accurately measuring target surface temperature with contact probes (as conduction

and convection effects can be significant), several methods have been developed to quantify T_{target} based on the spectrometric measurements themselves (Cheng et al., 2007). For outdoor measurements, the Iterative Spectrally Smooth Temperature/Emissivity Separation (ISSTES, Borel, 1998) based on atmospheric absorption lines is an apparently well performing approach (Horton et al., 1998; Cheng et al., 2007). For the current laboratory-based study the *blackbody fit* method (Kahle and Alley, 1992) was used. This assigns an emissivity value (local maximum) in a certain wavelength range, and by varying the assumed temperature in the emissivity retrieval process, the surface temperature that results in the best fit to this pre-defined emissivity value is determined. Expected values (Table 2) were derived based on:

- Spectra of similar materials from other libraries.
- Emissivity spectra had to remain below unity within the region 9–14 μm.
- For most samples additional outdoor LWIR spectral radiance observations were available (Kotthaus, 2014). Processed using the ISSTES method, these data provided information about the location and magnitude of the local spectral maxima.
- Complex material classes such as cement/concrete or metal were characterised by multiple reference points.

3.3. Impervious construction materials

Construction materials used for roads, pavements, building walls and roofs in London were studied using the measurement techniques described herein. Given *in situ* measurements cannot fully cover the immense variety of urban surface materials, the samples analysed are grouped into classes (Table 3). While most classes relate to fabricated materials, some natural impervious materials (e.g. granite or sandstone) are also included as they represent common constituents of composite construction materials such as asphalt and concrete. Other natural materials (e.g. vegetation, soils) play an important role in urban areas, however, they are usually well represented in existing spectral libraries and hence not studied here. Each sample analysed was coded with a material class ID (Table 3) plus sample ID (numerical). The initial classification based on usage and composition consists of ten classes with some refined into sub-classes (Appendix B). Composition was determined from labels, visual inspection and spectral response.

4. Results and discussion

First the sources of uncertainty in the laboratory-based spectral emissivity measurements are presented (Section 4.1), including tests of both the measurement system performance and the methodology. Then the derived emissivity spectra are presented and discussed (Section 4.2) along with VIS–SWIR reflectance spectra of the same samples.

4.1. Methodology evaluation of long-wave infrared spectroscopy

Radiometric calibration describes conversion of the recorded energy spectrum in raw DN to spectral radiance units (Section 3.2.2.1). The accuracy of the 2BB-method depends on the thermal uniformity and accuracy of the calibration sources, the linearity between recorded energy spectrum and observed radiance, and the temporal stability of the instrument response (gain) and self-emission. These are investigated in turn below and compared to the uncertainty of the estimation of the target temperature using the BB-fit approach (Section 3.2.2.3).

4.1.1. Thermal properties of the calibration blackbody system

Thermal properties of the flat plate blackbodies used to calibrate the FTIR data were evaluated using a handheld thermal imaging camera. To ensure the accuracy of this information, measurements made by the imager were first compared to a high quality cavity radiation standard with a small aperture and high spectral emissivity ($\varepsilon > 0.99$ across the LWIR wavelength range). The measured thermal imagery brightness temperatures were very close to the 'true' kinetic temperature of the cavity emitter (Fig. 1a), and the slight difference derived from the linear best fit was applied to all the subsequent thermal imager data.

The thermal imager was then used to collect data of the flat plate BB sources at a series of nine different temperatures, ranging from 40 °C to 100 °C and representing approximately equal spectral radiance intervals (Fig. 1b). The thermal image brightness temperatures were compared to the controller temperature to assess how closely the latter resembles the actual surface emission temperature (Fig. 1b). Applying the calibration relation derived for the thermal imager (Fig. 1a) and converting brightness into kinetic temperature estimates by accounting for the emissivity of the BB system, a good agreement was established (Fig. 1b). The derived relation was applied to all observations of the BB systems used in this study. During the analysis the two BB sources (Section 3.1.2) were found to have very similar thermal responses, so that only results from the first source (BB1) are shown here.

In this study, the FTIR FOV approximately covered the central 30 mm × 30 mm of the flat plate BB radiation sources so that an assessment of their thermal spatial homogeneity was warranted. With the radiation sources set to a fixed temperature (e.g. 76 °C shown in Fig. 2; similar behaviour at other temperatures) the edges of the blackbody aperture showed strong temperature gradients over a distance of about 5 mm (Fig. 2a). The blackbody source was a little cooler towards the edges, and thermal gradients differed slightly between the vertical and horizontal direction (solid lines, Fig. 2a). This could be attributed to spatial variations of the heating of the BB area, however, some impact might also arise from directional viewing effects and reflected down-welling radiance. The latter adds small contributions to the observed temperature because the radiation source is not quite a perfect blackbody but rather has an emissivity of 0.96 (Section 3.1.2). Either way, the spatial distribution of surface brightness temperatures observed using the thermal imager represents the thermal characteristics generally 'viewed' by the FTIR in the current setup.

If positioned accurately, the FOV of the spectrometer covers the central area of the BB radiation source (B, Fig. 2b; circular FOV approximated here by rectangular subset). If the FTIR is placed closer to the BB, the observed area is smaller (subset A) with marginally lower spatial temperature variability. Given the slightly cooler temperatures at the right edge of the source, a small decrease of $\overline{T}$ (increase of σ) across the area occurs when the distance between the BB source and the FTIR is increased (larger FOV, subsets C–D, Fig. 2b). If the viewing direction slightly differs from nadir, the FOV shifts to the side (subset E or F). These statistics reveal that average brightness temperature varies by less than 0.15 °C if an area of the blackbody within the central 16 cm^2 is viewed and thermal variability across the tested areas is small ($\sigma < 0.02$ °C). Being almost one order of magnitude lower than the temperature resolution of the BB temperature control unit (0.1 °C) these spatial variations introduce negligible errors. At 8–14 μm and the moderate temperatures considered here a temperature difference of 0.15 °C equates to a difference in Planck radiance (Eq. (1)) of only ~0.02 W m^{-2} μm^{-1} sr^{-1}, and the homogeneity of the BB radiation sources is therefore assumed sufficient within the central area. A comparison (not shown) of raw DN observed by the FTIR of the BB source at a central viewing direction and displaced to the left and to the right (similar to subsets E and F, Fig. 2b) confirms that

Table 2
Emissivity maxima ε_{max} and their locations defined by wavelength range [λ_{min}–λ_{max}] for the selection of impervious urban materials studied, used as input in the blackbody fit method.

Material	ε_{max}	λ_{min} [μm]	λ_{max} [μm]
Asphalt	0.975	12.0	12.5
Tarmac	0.970	11.5	12.0
Cement brick	0.975	12.0	12.5
Clay brick	0.975	7.5	8.5
Clay brick with beige paint	0.950	9.0	10.0
Clay brick with white paint	0.975	12.0	12.5
Clay brick with cement	0.975	12.0	12.5
Cement	0.960	9.5	10.5
Cement	0.960	10.5	11.5
Cement	0.950	11.0	11.5
Concrete	0.975	12.0	12.5
Granite	0.975	12.0	12.5
Roofing shingle	0.960	12.0	12.5
Ceramic roofing tile	0.950/0.975	12.0	12.5
Cement roofing tile	0.975	12.0	12.5
Limestone	0.940	9.5	10.5
Sandstone	0.975	12.0	12.5
PVC roofing sheet	0.960	11.0	12.0
Aluminium plus zinc	0.850	10.0	11.0
Stuccoed aluminium	0.050	8.5	9.5
Metal with paint	0.970	10.5	11.5
Lead	0.940	8.0	9.0
Black iron	0.970	9.0	10.0
Quartzite conglomerate	0.97/0.95	12.0	12.5
Silica sand	0.975	12.0	12.5

Table 3
Classes of impervious urban materials analysed from London.

Material class	Class ID	Sub-class	Number of samples
Quartzite	X	Quartzite conglomerate	3
Stone	S	Sandstone	3
		Limestone	2
Granite	G	Granite	5
Asphalt	A	Road asphalt	9
		Asphalt roofing paper	1
Concrete/cement	C	Concrete	4
		Cement	3
Brick	B	Clay brick	7
		Cement brick	7
Roofing shingle	L	Roofing shingle	4
Roofing tiles	R	Ceramic roofing tile	7
		Concrete roofing tile	5
Metal	Z	Metal	5
		Metal, painted	3
PVC	V	PVC	6

the response is similar within the central 16 cm^2, but changes when parts of the BB are sampled that are more than 20 mm away from its centre.

4.1.2. Linearity of instrument response

Assuming the response of the spectrometer to incoming radiance is linear (Section 3.2.2.1), then the gain (slope) and instrument self-emission (intercept; Eq. (5)) can be obtained from the recorded energy spectrum in raw DN and the incoming radiance calculated from the flat plate blackbodies, both changing as a function of wavelength.

To evaluate this presumably linear relation, raw DN recorded by the FTIR system during observation of the blackbodies at 40–100 °C (solid lines in Fig. 3) were analysed in relation to the theoretically expected Planck radiance (Eq. (1)) at these temperatures (dashed lines), taking into account the BB emissivity of 0.96. While the theoretically expected radiance decreases with increasing wavelength across the 8–14 μm region, the recorded raw DN curves have a concave shape with a maximum between 10 and 11 μm (Fig. 3). This illustrates the instrument's changing relation between raw DN and incoming radiance across the LWIR wavelength range.

The same data (as Fig. 3) illustrate that, at a given wavelength (e.g. 9 μm), BB radiance can be expressed as a function of the measured raw DN signal across the observed temperature range (Fig. 4). Using observations at all nine temperatures, instrument self-emission (intercept) and gain (slope) are estimated (dashed lines, Fig. 4). The small root mean square errors (RMSE: 0.26–0.07 W m^{-2} μm^{-1} sr^{-1} for 8–14 μm) confirm that the relation between raw DN and incoming spectral radiance appears to be well approximated by a linear function. To test the accuracy of this relation, a third (independent) BB radiation source ($\varepsilon = 0.96$) was observed at eight different temperatures, along with the flat plate calibration blackbodies. With the target BB heated to about 50–60 °C, the flat plate BB sources for radiometric calibration were set to 40–45 °C and 70 °C respectively. The detected energy spectrum from the target BB source was calibrated from raw DN to radiance units using the linear regression equation obtained from all nine measurements of the flat plate BB sources (as in Fig. 4); and by choosing 20 combinations of two different temperatures selected from the set of nine temperatures (T_{BB1} = 40–76 °C; T_{BB2} = 82–98 °C).

Generally, this radiometric calibration yields radiance values very close to the theoretically expected Planck radiance for the independent target (Fig. 5, solid lines). The spectral RMSE describing the linear fit at each wavelength is shown as the shaded area, providing an indicator of the uncertainty. Especially well represented is the radiance at temperatures in the range important to the current study (50–60 °C), while radiance at higher temperatures (65.8, 72.1, 78.9 °C) appears overestimated between 8 and 10 μm or underestimated (84.5, 89.1 °C) above 10 μm. Below wavelengths of 8 μm, the calculated radiance starts to deviate distinctly from the expected values suggesting that the linearity of the relation between raw DN and incoming spectral radiance becomes invalid. Fortunately, measurements at these wavelengths are not used in the current analysis, in part because they are outside the 8–14 μm atmospheric window.

When calibration is based on BB observations at only two temperatures (20 combinations tested here, dashed lines, Fig. 5), the calculated radiance generally agrees with the expected function in terms of shape and magnitude, however, some uncertainty is evident. The radiance retrieved for the lower temperature target (e.g. 38.5 °C) has a particularly larger spread. Presumably, coefficients derived from two higher temperatures do not represent an accurate calibration function for a colder target. This again supports the assumption that the 2-BB method works best if the BB sources are set to temperatures closely bracketing the temperature of the target. With this setting, the errors introduced by the calibration remain small (mean bias error between 8 and 14 μm: 0.06 W m^{-2} μm^{-1} sr^{-1}), hence it is used for all subsequent observations in this study.

4.1.3. Stability over time

Sampling the target spectral radiance multiple times improves the signal-to-noise ratio, but the measurement situation must remain static during this period. To balance these priorities, ten samples were chosen to allow a reasonably quick measurement period (~2 min). To estimate how stable the whole measurement environment remains during one set of observations, the calibration sources, an independent BB source (at 55 °C) and the gold reference panel were sampled ten times, resembling the sampling strategy used for the target measurements (Section 3.1.2). The raw

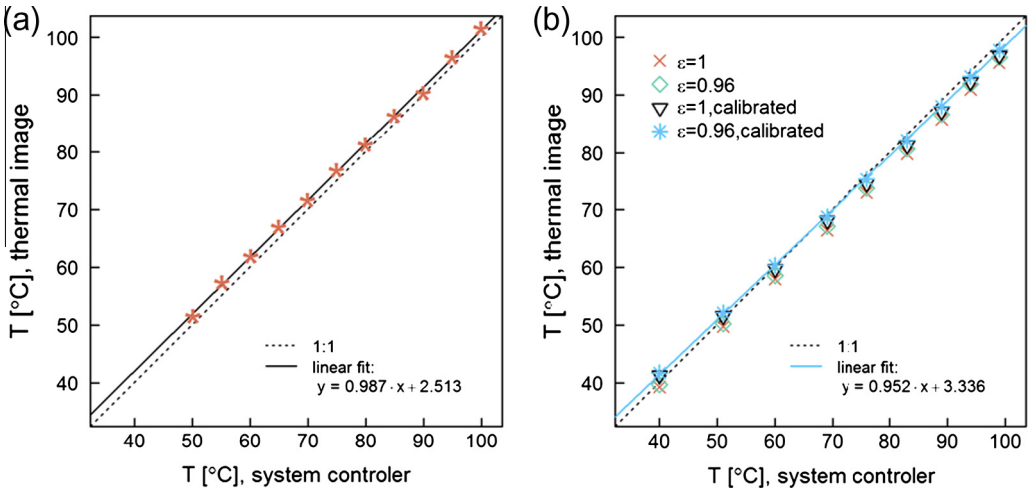

Fig. 1. Measured radiometric temperature from the thermal imager as a function of blackbody (BB) body temperature, as displayed by the BB system controller for (a) a high emissivity ($\varepsilon > 0.99$) cavity radiation standard and (b) a 'flat plate' BB radiation source ($\varepsilon = 0.96$) later used for FTIR calibration. Both are observed with the same LWIR (8–14 μm) thermal imaging camera. In (b) four settings illustrate the impact of adjusting the LWIR brightness temperature measurement of the thermal imaging camera for the non-unitary emissivity of the target, and of taking into account the adjustment to the thermal imager calibration shown in (a).

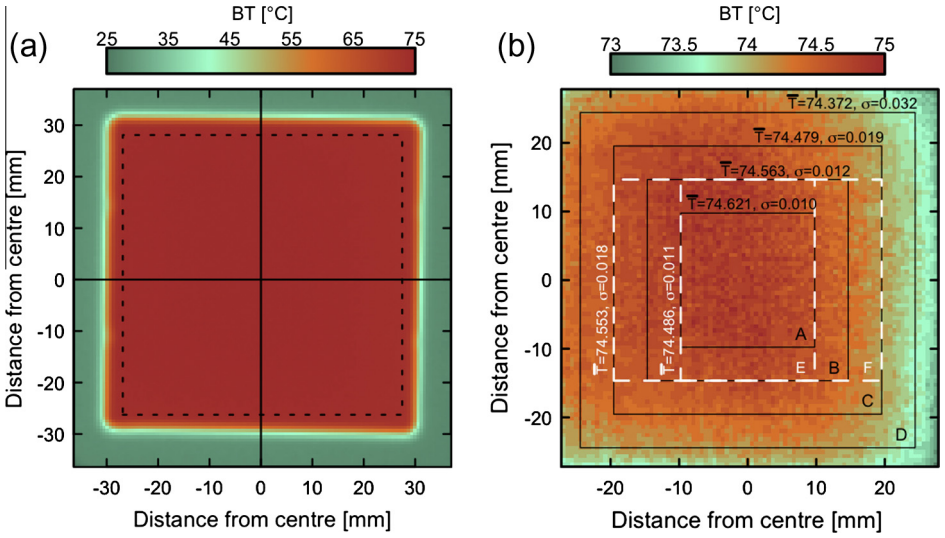

Fig. 2. Brightness temperature (BT) imagery of flat plate blackbody (BB1) at a system controller temperature of 76 °C recorded using the LWIR (8–14 μm) thermal imager described in Fig. 1. (a) Whole aperture; solid lines: selected cross sections; dotted line: subset without strong edge effects (cf. b); (b) central area of flat plate BB; solid/dashed lines: subsets of varying size/location. Given the high spatial resolution of the image (mean pixel size = 0.6 mm × 0.6 mm), no adjustment is applied to account for small variations in pixel size across the image when calculating areal statistics of mean brightness temperature ($\overline{T}$) and standard deviation (σ).

DNs were converted using one set of calibration measurements with BB temperatures of 40 and 70 °C. To account for self-emission from the InfraGold, the gold radiance was converted to incoming radiance (Eq. (8)).

Firstly, temporal variability of both instrument self-emission and gain (Eq. (5)) are evaluated (Fig. 6), both clearly varying as a function of wavelength. As standard deviations of both estimates reveal, calibration is most stable for the 9–11 μm spectral region, and increases below 8.5 μm and above 11 μm. This is associated with the convex-shaped spectral pattern of the detected energy spectrum itself (raw DN in Fig. 6), presumably indicating a better signal-to-noise ratio in the centre of the LWIR region for the temperatures used here. Particularly increased noise is identified between 8.6 and 9.0 μm.

At a timescale of about 2 min (i.e. time to collect 10 samples) both the radiance reflected by the reference panel and that emitted by the independent BB varied only slightly (Fig. 7): by approximately 0.3% and 0.6%, respectively. Temporal variability of the calibrated radiance (spectral standard deviation of 10 measurements) is clearly related to the calibration coefficients (cf. Fig. 6), with a more stable region between 9 and 11 μm. The error propagation is less pronounced above 11 μm, where the increase in standard deviation of instrument emission and gain is less evident in the standard deviations of the final calibrated radiance values of both blackbody target and incoming radiance (Fig. 7). The overall uncertainty (RMSE between 8 and 14 μm: 0.02 W m^{-2} μm^{-1} sr^{-1}) introduced by these temporal variations is lower than that linked to the assumption of calibration relation linearity (Section 4.1.2). However, as the two sources of measurement error are related they cannot be quantified completely independently via the means available here.

4.1.4. Evaluation of the emissivity retrieval method

The experimental setup plus retrieval method for the measurement of long-wave emissivity spectra was assessed using a sample

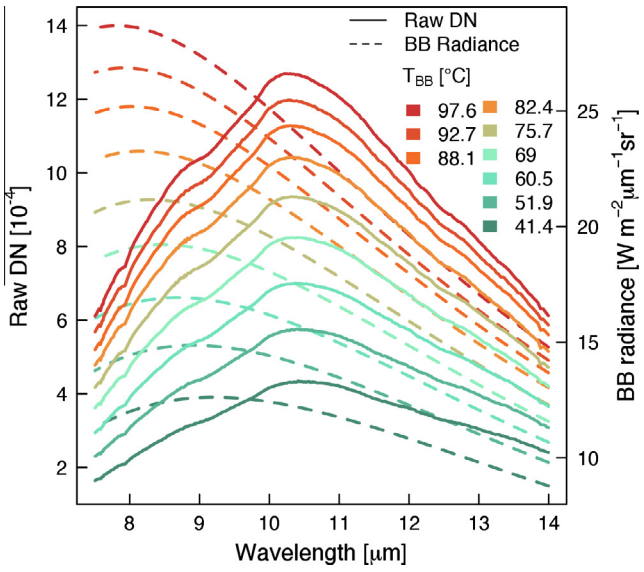

Fig. 3. Raw digital numbers (DNs) recorded by the MIDAC FTIR system when observing the flat plate blackbody (BB1) of Fig. 2 from a distance of 10 cm (BB2 is similar but not shown). Observations at a series of different temperatures T_{BB} (as displayed by the BB controller unit) are shown, along with the respective spectral radiance curves deduced using the Planck function (Eq. (1)) and the BB emissivity of 0.96.

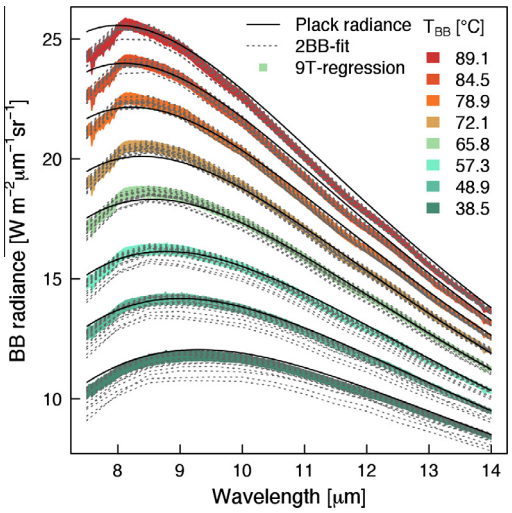

Fig. 5. Blackbody spectral radiance of an independent radiation source at different temperatures (T_{BB}), calibrated using the observations of the flat plate black bodies at nine temperatures (9T) (see Figs. 3,4): shaded area: spectral radiance calculated via the application of the linear calibration relations derived through all nine BB observations ± spectral root mean square error, dashed lines: spectral radiance calculated from linear calibration relations derived through observations at 20 combinations of two selected BB temperatures, and solid lines: expected values according to the Planck Function ($\varepsilon = 0.96$). Statistics (see text) calculated for thermal infrared region 8–14 µm.

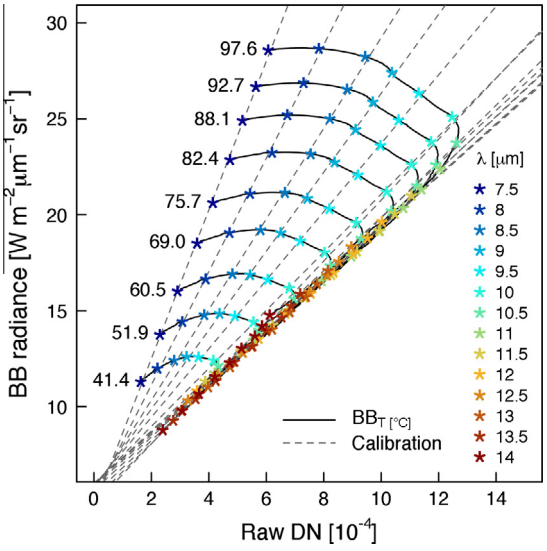

Fig. 4. Spectral radiance as calculated for the flat plate blackbody system (BB1 (whose data are shown in Figs. 1-3); BB2 similar, not shown) with $\varepsilon = 0.96$ at different temperatures T (labelled [°C]), displayed against Raw DN (digital numbers) recorded by the MIDAC FTIR system when observing the same BB source. Linear relations, that define the radiometric calibration between raw DN and spectral radiance, are shown for a series of selected wavelengths (dashed lines).

of known composition (Fig. 8). A quartz sample (Ottawa silica sand) was chosen as a reference given its clear and well pronounced reststrahlen features (Salisbury and D'Aria, 1992).

To separate the emissivity information contained within the spectral radiance measurements from the kinetic temperature, the blackbody fit method (Section 3.2.2.3) was applied. This introduces uncertainty as *a priori* knowledge about the target's spectra is required (Table 2). While the wavelength location of the local emissivity maximum can be specified as an approximate band, its actual magnitude (e.g. 0.985 between 12.0 and 12.5 µm for the Ottawa silica sand sample) needs to be rather accurately known as this can directly impact the results. An error of ±0.01 in this emissivity value causes a temperature error of ~0.5 °C and hence introduces uncertainty to the specified Planck radiance (shading around dashed line in Fig. 8, top).

The discussed measurement errors linked to the radiometric calibration (Sections 4.1.2 and 4.1.3) could accumulate to a spectral measurement uncertainty of around 0.08 W m^{-2} µm^{-1} sr^{-1} in the final calibrated target radiance (denoted by the shading around the solid line in Fig. 8, top). Conversion to spectral emissivity illustrates (Fig. 8, bottom) that the total uncertainty expected from radiometric calibration and system performance have an impact comparable to an uncertainty of ±0.01 in the maximum specified emissivity.

The retrieved spectrum of the silica sand compares well to that from the ASTER spectral library (Ottawa silica sand, Baldridge et al., 2009; Fig. 8, bottom). The ASTER library data are mostly within the range of uncertainty specified for the sample measured here (LUMA). Only around the emissivity minima does the ASTER spectrum differ (being slightly lower). Furthermore, the two spectra have the same integrated broadband emissivity of 0.85 (difference = 0.003). This proves that under controlled laboratory conditions the tested portable FTIR system and radiometric calibration setup can be used to collect high quality emissivity spectra.

4.2. Spectral response of impervious urban materials

VIS–SWIR reflectance spectra and LWIR emissivity spectra of 74 material samples obtained from construction sites across London are studied. These materials are grouped into ten classes according to appearance and usage (Appendix B) and derived broadband albedo and emissivity are provided (Appendix C, Table C.1). The results of this study are available as an online spectral library of impervious urban materials (SLUM) within the London Urban Micromet data Archive (LUMA, http://Londonclimate.info/LUMA/SLUM.html). Here, the spectra most representative of the material classes studied are presented graphically, while others are put into context (Section 4.2.1). Given the similarity of spectral signatures

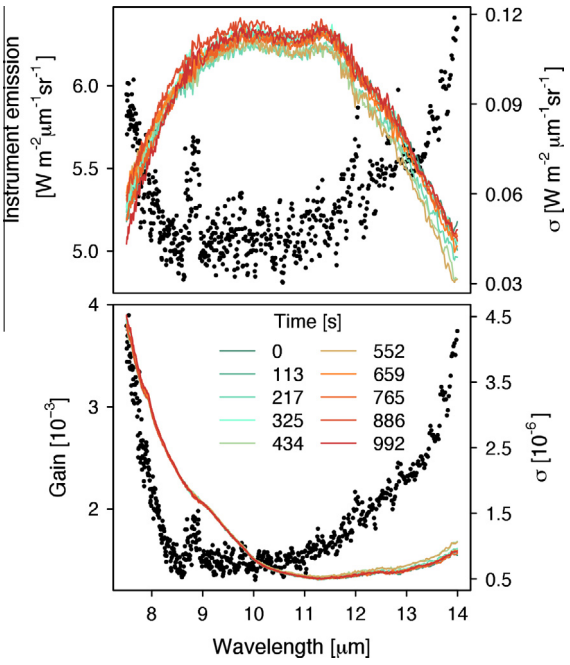

Fig. 6. Radiometric calibration coefficients for the MIDAC FTIR spectrometer system, describing the linear relation between the measured energy spectrum in raw DN and the spectral radiance (Eq. (5)): (top) instrument self-emission (S_λ); and (bottom) gain (G_λ). Coefficients derived from ten subsequent measurements of two flat plate BB sources at 40 °C (BB1) and 70 °C (BB2), respectively, using the method described (Section 3.2.2.1); (dots) respective standard deviations across the ten samples. Legend lists time-difference since first measurement.

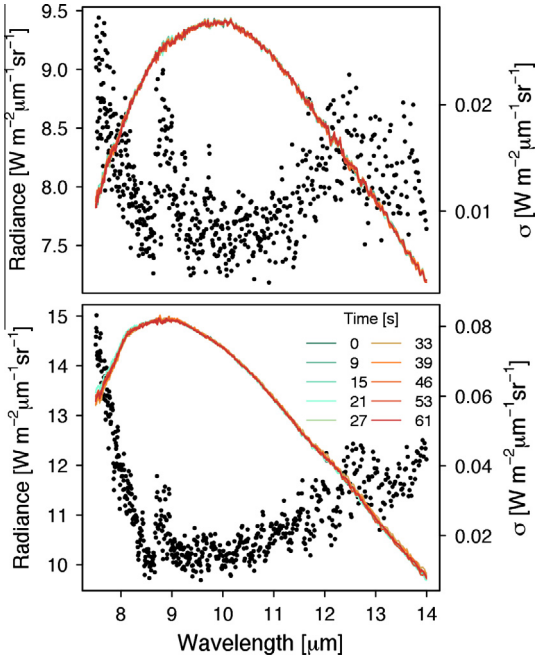

Fig. 7. Temporal variability in the calibrated spectral radiance over the course of ten contiguous measurements (solid lines), displayed as normalised standard deviation (dots) of (top) incoming spectral radiance as characterised by observations of the gold reference panel, and (bottom) calibrated spectral radiance emitted by an independent blackbody target ($\varepsilon = 0.96$). Observations are calibrated into spectral radiance using a single set of calibration blackbody measurements made just before the first measurements. Legend lists time-difference since first measurement.

of certain materials across classes, these are then grouped according to their LWIR radiative response (Section 4.2.2). A combination

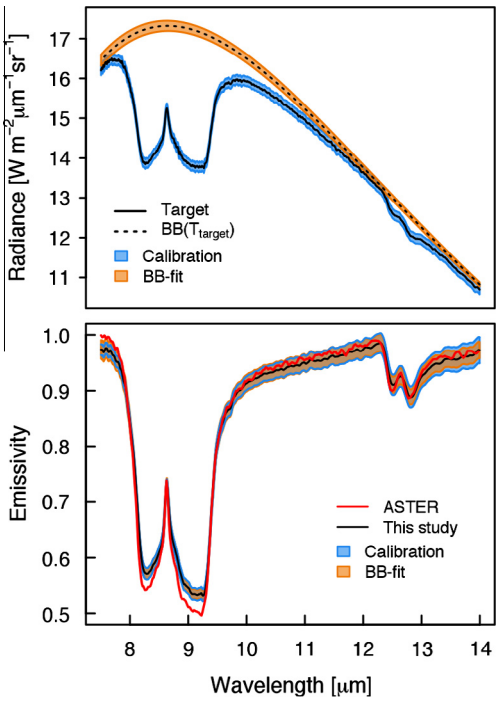

Fig. 8. Observations of silica sand (Ottawa) taken with the MIDAC FTIR system (described in this study) deployed in the laboratory: (top) calibrated spectral target radiance and theoretical Planck radiance of a blackbody at the same temperature (T_{target}), (bottom) spectral emissivity derived from these measurements (cf. top) along with reference spectrum from the ASTER spectral library (Baldridge et al., 2009). Shading indicates uncertainty linked to radiometric calibration and BB-fit method, respectively.

of both classification approaches appears most appropriate to characterise the complex urban surface composition.

4.2.1. Characteristics of the impervious urban materials studied

4.2.1.1. Quartzite conglomerate. As feldspar and quartz do not create specific absorption features in the short-wave region, the reflectance spectrum of the quartzite conglomerate sample (X001; Fig. 9a) reveals a somewhat unexpected pattern. The locations of the strongest features (i.e. 1700 and 2300 nm) suggest contributions of hydrocarbons (C–H combinations; King and Clark, 1989) such as found in industrial solvents (e.g. benzene, toluene, and trichlorethylene; van der Meer and Jong, 2002). Hence, it is speculated these absorption bands maybe attributed to the influence of the binder applied to fix the quartzite grains. Spectral emissivity of the quartzite conglomerate (Fig. 9b) appears to be less affected by that binder, as its shape is clearly dominated by the characteristic quartz doublet (Fig. 8). Still, the overall magnitude of the LWIR emissivity may be affected.

LUMA samples of quartzite conglomerates vary in grain size and colour. Their short-wave reflectance spectra reveal the same absorption bands; however, one sample has a higher reflectance overall. In terms of spectral emissivity, the additional samples (X002; X003) differ from the one presented (X001) being dominated by a constantly high emissivity leaving no evidence of any reststrahlen effects. The binder materials in the conglomerate may again explain this. Further information on the composition would be required to understand why the binder does not dominate the LWIR spectrum of the X001 sample. The measurements have been repeated, both in the lab and in the field (see Appendix Afor methodology), in order to eliminate measurement errors as the cause of this difference.

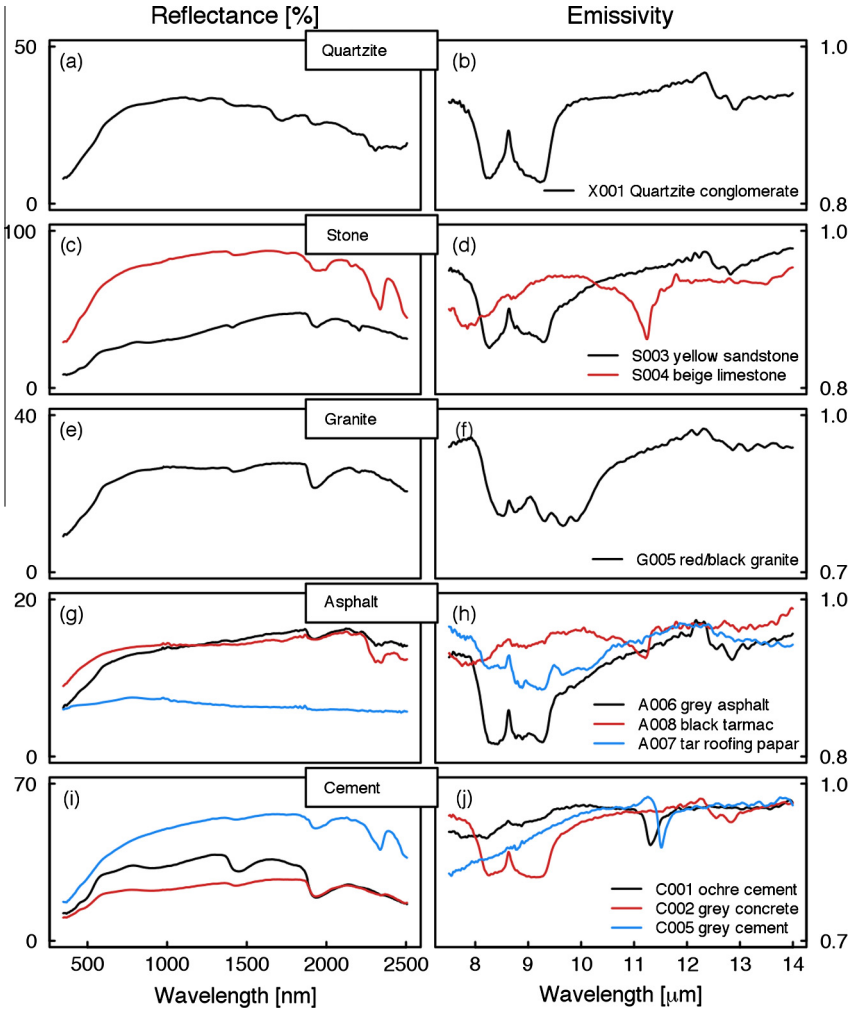

Fig. 9. Examples of (left) absolute VIS–SWIR reflectance spectra and (right) absolute LWIR emissivity spectra for five classes of impervious urban materials (Section 3). Spectra determined using the SVC HR2014 (VIS–SWIR) and the MIDAC FTIR system (LWIR) (described Section 2) deployed in the laboratory.

4.2.1.2. Stone. In the VIS–SWIR, the beige limestone (S004; Fig. 9c) has a very high overall reflectance and shows strong absorption at the characteristic 1900 and 2350 nm (and presumably 2550 nm) wavelengths. The sandstone sample (S003; Fig. 9c) reveals contributions of both iron oxides as well as clay minerals, with the pronounced H_2O absorption at 1900 nm suggesting a smectite mineral (potentially montmorillonite). Clearly more distinct are the characteristics of the two stones in the LWIR region (Fig. 9d). While limestone can be identified based on its characteristic reststrahlen band at around 11.3 μm, the spectral emissivity of sandstone is close to the quartzite signature (Fig. 9b).

The LUMA spectral library includes other samples in the stone material class (not shown; Appendix C, Table C.1). The grey carboniferous limestone (S002) shows only weak absorption features and has a much lower overall reflectance than the beige limestone (S004). Spectral emissivity is more similar, but again, the carboniferous limestone has a weaker reststrahlen signature. The two additional sandstone samples (S001; S005) have a very similar response as the presented samples (S003) across both the short- and long-wave regions.

4.2.1.3. Granite. VIS–SWIR reflectance spectra of the granite samples do not show particular characteristics, apart from a broad H_2O absorption feature at 1900 nm. The sample presented (G005; Fig. 9e) is the one with the lowest albedo. The LWIR response of the various granite samples differ slightly, however, as for the sample shown (G005; Fig. 9f), all resemble some combination of quartz and feldspar spectra. Superimposed over the quartz reststrahlen bands (forming the doublets between 8.0–10.0 μm and 12.3–13.0 μm) are the absorption peaks of feldspar at 9.0, 9.5, and 9.8 μm (Christensen et al., 2000).

4.2.1.4. Asphalt. The VIS–SWIR spectra of the weathered road asphalt and tarmac samples (A006 and A008; Fig. 9g) are typical of dark hydrocarbon materials, i.e. reflectance is quite low overall (note varying *y*-axis scale in Fig. 9) and slightly increases with wavelength. The tar roofing paper (A007; Fig. 9g) is coated with slate chippings that cause low reflectivity (cf. L001d; Fig. 10c). Due to the strong hydrocarbon absorption, long-wave emissivity of asphalt and tarmac is generally high (A006 and A008; Fig. 9h). Materials with high aggregate fractions at the surface (e.g. asphalt sample A006) show the associated absorption features (of e.g. granite or quartz) in their spectra, while hydrocarbon absorption dominates the response of those with smaller aggregate contributions (e.g. tarmac sample A008). The feature at around 11.3 μm of the black tarmac sample (A008) indicates contributions from carbonate minerals that would explain the increased absorption at 2350 nm found in its VIS–SWIR reflectance spectrum (Fig. 9g). In agreement with its VIS–SWIR radiative response, LWIR emissivity of the asphalt roofing paper (A007; Fig. 9h) has characteristic slate

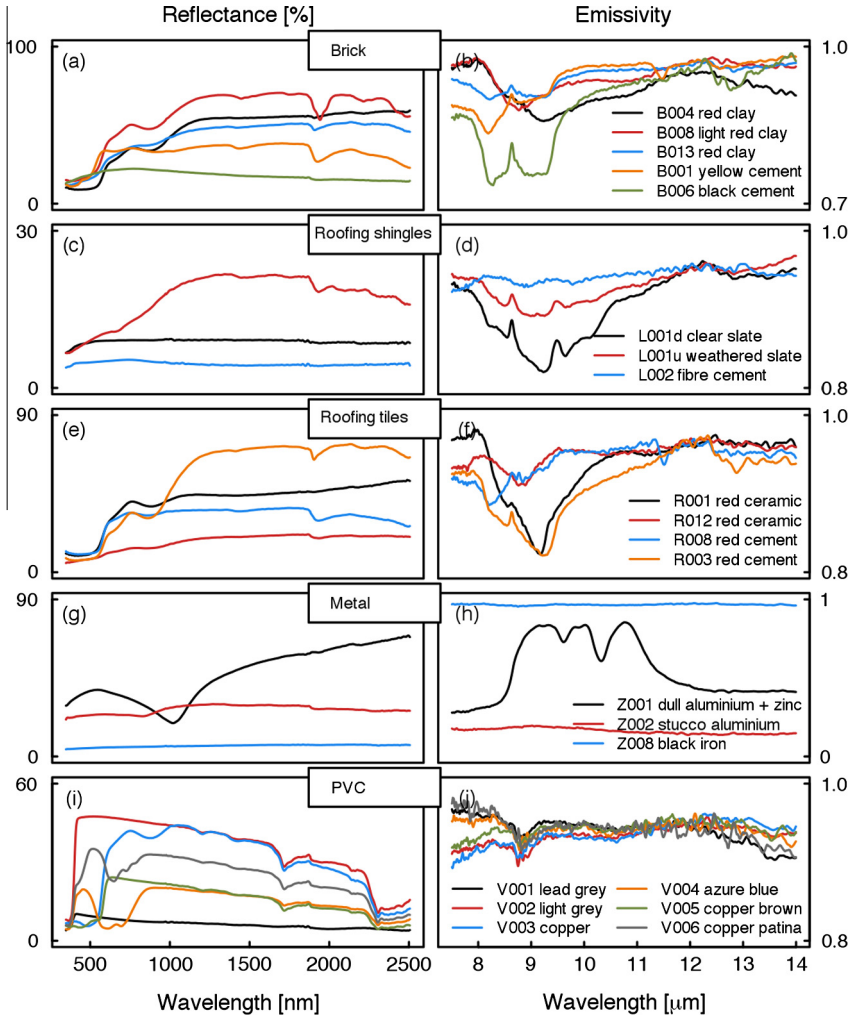

Fig. 10. As for Fig. 9 for additional material classes.

features (cf. L001d; Fig. 10d). A range of additional asphalt and tarmac material samples are included in LUMA SLUM (Appendix C, Table C.1). Their broadband response in both regions differs with the amount of aggregate. As all samples were exposed (weathered, dirty, dusty) to London's atmosphere, this probably also affects their spectral characteristics.

4.2.1.5. Concrete and Cement. Cement and concrete are both composed of variations of silica and carbonates, possibly with other minerals and rocks contributing to concrete materials. Here, materials dominated by quartz signatures in their long-wave radiative response are classified as concrete, whereas the remainder are assigned to the cement category. However, it should be noted that the two materials are very similar (given cement is the main constituent of concrete) with the relative amounts of siliceous and calcareous minerals governing their spectral radiative response.

All VIS–SWIR spectra of the cement/concrete class exhibit a reflectance increase up to about 600–700 nm, and strong absorption around 1940–1970 nm (Fig. 9i). The latter indicates H_2O related absorption of the gypsum component. As seen in the spectrum of the ochre cement sample (C001) some cement and concrete materials have signatures of iron oxides or absorption at other H_2O related bands (e.g. around 1410 nm). The grey cement (C003) spectrum again shows a deep reflectance minimum around 2310–2350 nm, which could represent C–H features characteristic of bitumen/asphaltic materials (Fig. 9g) or carbonate features known from limestone.

The absorption/reststrahlen features of cement and concrete differ distinctly across the LWIR. Given their congruence in mineral-composition, LWIR spectral emissivity of cement (carbonate dominated) and concrete (quartz dominated; Fig. 9j) is generally similar to that of limestone and sandstone (cf. Fig. 9c; note varying *y*-axis scale in Fig. 9), respectively. While the emissivity of the grey cement sample (C003) closely resembles that of pure limestone, with a pronounced minimum at 11.3 μm, the quartz-doublet reststrahlen feature dominates the spectra of the concrete samples (C002). The emissivity spectrum of the ochre cement sample again (C001) is formed of a superposition of absorption features of these two minerals. The clear carbonate reststrahlen signature of the grey cement sample (C003) indicates that the short-wave absorption band around 2310 nm (Fig. 9i) is also attributed to this mineral.

4.2.1.6. Brick. Bricks made of clay or cement both hold some hydroxyl and water related absorption in the VIS–SWIR (Fig. 10a). Clean clay brick samples show very strong absorption up to 520 nm, with further signatures at 670 and 870 nm, as is characteristic for iron oxides (B004; B008; B013). However, the yellow cement brick sample (B001) also shows signatures that could be linked to iron oxide absorption (Fig. 10a), suggesting that these features cannot

be used to reliably distinguish between ceramic and cement materials. The depth of the iron oxide features varies between the samples, possibly due to weathering effects. The black cement brick (B006) has a constantly low reflectance. Generally, the clay brick samples in this study have a higher overall reflectance than those made of cement.

Differentiation between cement and ceramic-based bricks is more obvious from their thermal response. The red clay brick sample (B004; Fig. 10b) has a near classic clay signature of diminished emissivity between about 8.0–12.0 μm (minimum at ~9.2 μm) while the black cement brick (B006) is dominated by silica features only. The spectrum of the light red clay brick (B008) also shows the response of clay minerals, however, emissivity is a little higher overall and the minimum is shifted to ~8.8 μm. The spectrum of the yellow cement brick sample (B001) indicates contributions from quartz as well as carbonate mineral reststrahlen effects, similar to the ochre cement sample (C001; Fig. 9j). The clay signature of the extremely weathered red clay brick (B013) is obscured because some remains of cement mortar on its surface clearly affect its LWIR emissivity spectrum, introducing the quartz reststrahlen doublet.

4.2.1.7. Roofing shingles. The clean slate roofing shingle (L001d) has a constant, low reflectance in the VIS–SWIR (Fig. 10c) with no evident absorption features. This signature is similar to that of the asphalt roofing shingle (Fig. 9g) coated with slate chippings. The fibre cement sample (L002; Fig. 10c) also has a very low, featureless reflectance, despite being weathered. The effect of weathering on the slate shingle is vast. Mostly due to moss, its reflectance is increased considerably (even doubled for some wavelengths) and some O–H absorption is introduced (L001u; Fig. 10c). Spectral emissivity of slate is formed by the spectral response of clay minerals and siliceous minerals. Superimposed over the quartz reststrahlen bands are the absorption characteristics of muscovite at 8.6, 9.4, 9.8, and 10.7 μm (Rodriguez et al., 1999). These features are evident in both slate samples (L001d and L001u; Fig. 10d), albeit with variations in the depths of the absorption troughs. Presumably, the moss on the weathered slate shingle (L001u) increases the emissivity. As in the SWIR region, the black fibre cement shingle is an efficient absorber in the LWIR, with no apparent absorption or reststrahlen bands in their emissivity spectra (L002).

4.2.1.8. Roofing tiles. The roofing tile short-wave spectra (Fig. 10e) confirm iron oxide features are often present in the spectral reflectance of both ceramic and cement tiles, supporting the conclusion drawn (Section 4.2.1.6) that the detection of these chromophores alone is not sufficient to distinguish ceramic materials. The overall reflectance of both materials varies greatly for the different samples of various colours. Generally, weathering appears to increase absorption in the VIS–SWIR for ceramic tiles, e.g. the weathered red ceramic tile (R012) compared to the new red ceramic tile sample (R001; Fig. 10e). The cement roofing tiles observed in the current study are all new materials (e.g. R008; R003), so the effect of weathering in this material class cannot be examined.

The roofing tiles exhibit a similar diversity as bricks (Fig. 10b) in the spectra of LWIR emissivity (Fig. 10f). Again, clay minerals shape the response of ceramics such as the new red ceramic tile (R001) while a combination of silica and carbonate minerals dominates the cement tiles (e.g. R003; R008). The reststrahlen effect of the clay minerals is diminished for the weathered red ceramic tile (R012) so that its overall emissivity is higher than that of the new red ceramic tile (R001) and the emissivity minimum is slightly shifted to shorter wavelengths. Generally, given all roofing tiles are manufactured, composite materials, they tend to have reststrahlen features of various minerals superimposed. For example, the quartz doublet of the red cement roofing tile (R008) is weakened by carbonate absorption so that the spectrum closely resembles that of the yellow cement brick (B001; Fig. 10b). Even in the emissivity spectrum of the red ceramic roofing tile (R001) a weak silica absorption signature at 8.6 μm can be identified. These combinations of absorbing minerals in the materials' compositions can make it difficult to find clear criteria for the classification of such materials given spectra within one sub-class can vary as much as between sub-classes. For example, the emissivity spectra of the two red cement tiles (R003; R008) more closely resemble the shape of the new red ceramic tile (R001) and the weathered red ceramic tile (R012), respectively, than one another.

4.2.1.9. Metals. Metal samples in the LUMA SLUM include new, weathered and painted samples. Spectra of VIS–SWIR reflectance of aluminium usually tend to increase with wavelength after a broad absorption dip at the respective characteristic locations. The grey/dull aluminium plus zinc sample (Z001) exhibits this characteristic shape (Fig. 10g) while the shiny/stucco aluminium (Z002) is rather featureless in the VIS–SWIR. Similarly, the black iron manhole cover (Z008) has a consistently low reflectance. The diversity of spectral signatures within the metal category is even greater in the LWIR, given materials with both extremely high and low emissivity are included (Fig. 10h). As in the VIS–SWIR, the black iron sample (Z008) does not show any spectral variations. Presumably, the dull aluminium/zinc sample includes some further constituents that generate its particular emissivity signature (Z001). As in the short-wave region, the latter clearly differs from that of the shiny, stucco aluminium (Z002).

4.2.1.10. PVC. The VIS–SWIR reflectance of PVC samples (Fig. 10i) shows that the dominant hydrocarbon absorption features are manifestly the same for all samples, apart from the slate-grey PVC (V001), which is again characterised by a particularly low reflectance throughout the whole VIS–SWIR region. The different colours of the PVC samples cause great variability in terms of reflectance for visible wavelengths. No LWIR emissivity spectra of PVC materials are available from the reference online libraries listed (Table 1). The spectral emissivity of the PVC roofing materials (Fig. 10j) is somewhat comparable to the signature of a weathered, red ceramic roofing tile (R012; Fig. 10f), with a local absorption minimum at ~8.8 μm. Depending on colour, PVC sheets exhibit an increase or decrease of emissivity at wavelengths shorter than 8.5 μm.

4.2.2. Classification of urban materials

The spectral observations provide additional information beyond optical appearance and usage of construction materials (Section 4.2.1). This allows for the impervious urban materials to be grouped by the constituents dominating the radiative response. Distinct absorption/reststrahlen features were identified in many LWIR spectra observed which allows most impervious materials studied to be grouped by their dominant chemical composition (Fig. 11). Metals, PVC and 'contaminated' materials (e.g. painted) are omitted from this classification due to their diversity and complexity.

In addition to the abundant quartz and feldspar, carbonate minerals are important given that limestone (consisting of calcium carbonate) is an essential ingredient of composite materials such as cement. Also other silicates (phyllosilicates) are frequently found in impervious urban construction materials (clay minerals: e.g. brick or roofing tiles; mica: e.g. slate roofing shingles or asphalt roofing paper). The dominance of these minerals on the radiative response becomes apparent in the comparison of the LWIR spectra (Fig. 11). Emissivity of the material samples analysed can be attributed to the controls of carbonates, phyllosilicates, quartz, or a combination of quartz plus feldspars or quartz plus carbonates. Only a

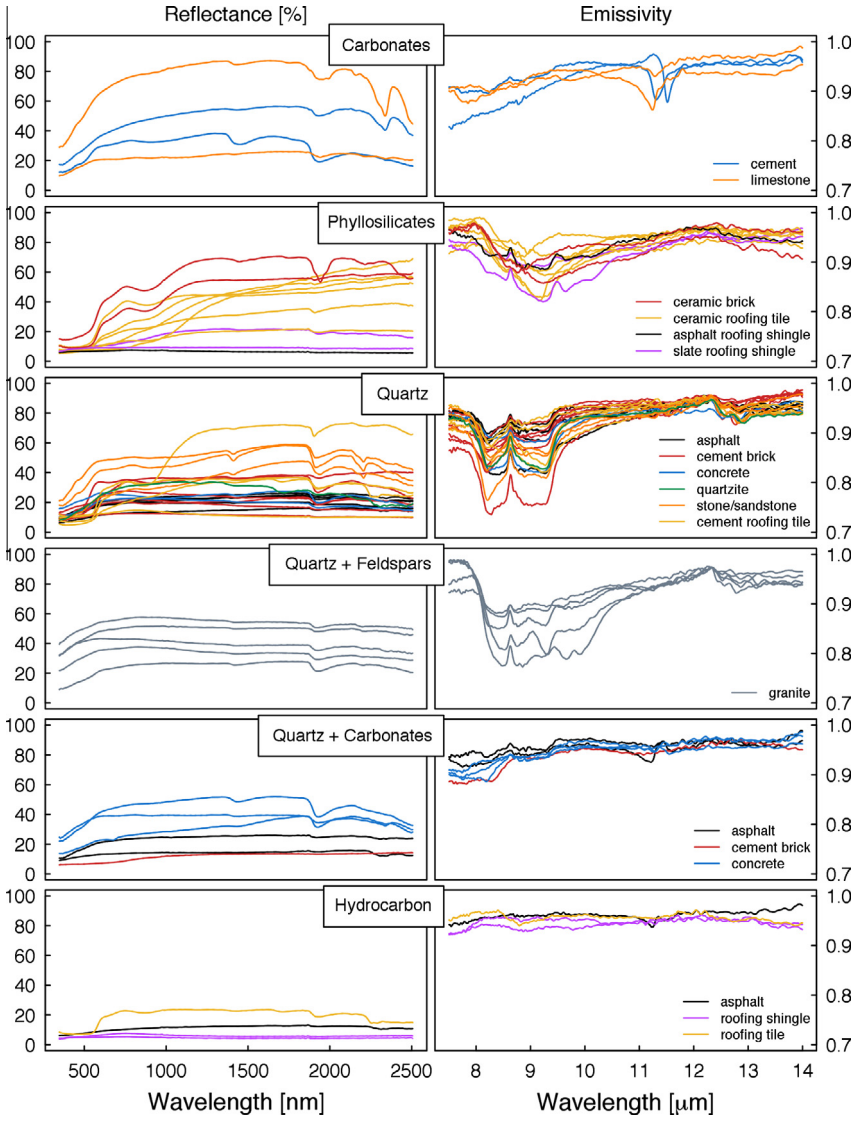

Fig. 11. As for Fig. 9 for impervious urban materials whose long-wave radiative response is dominated by carbonates, clay minerals (phyllosilicates), quartz minerals, quartz plus feldspar, quartz plus carbonate or hydrocarbons.

few materials with featureless spectra are presumably governed by hydrocarbons.

The VIS–SWIR reflectance spectra show some similarities within these mineral groups, however, distinct features are rare (e.g. carbonate) and not always unique to one group (e.g. iron oxide features). This demonstrates clearly the potential of hyperspectral LWIR data for characterising impervious urban surface materials.

5. Conclusions

This study presents one of the first spectral libraries of impervious urban materials covering both the VIS–SWIR and the LWIR spectral regions. Data from 74 samples were collected using field-portable spectrometers in controlled laboratory conditions with methodologies mostly applicable also to an outdoor setup. All spectra are combined in the online spectral library of the London Urban Micromet data Archive (LUMA; http://LondonClimate.info/LUMA/SLUM.html).

A detailed framework for the spectral emissivity measurements using a field-portable FTIR spectrometer was developed. It was demonstrated how uncertainties linked to the instrumental setup and radiometric calibration can be assessed using a thermal imaging device and auxiliary observations from independent radiation sources. In order to ensure a suitable signal-to-noise ratio, targets observed under laboratory conditions need to be heated substantially above room temperature immediately prior to the spectral sampling (not necessary outdoors). The methodology and setup were evaluated by measuring a sample of known composition (Ottawa silica sand), revealing that errors from radiometric calibration and system performance have a comparable impact as those linked to the approach taken to separate the temperature and emissivity signature of the target.

The short-wave response of composite construction materials varies greatly, whilst the long-wave response is more consistent within a single material class. Given that many materials consist of minerals, which often have very distinct reststrahlen and absorption features in the LWIR, hyper-spectral information in this spectral region offers great potential to aid in the characterisation of these constituents. In the UK, sandstone, concrete and brick are common building materials in residential and many central urban areas. Although common construction materials were the focus of analysis in this study, these are insufficient to represent all urban surfaces. Thus, more work is required to adequately characterise

metals (e.g. industrial land use or high rise central business districts), new building materials such as PVC, and also painted surfaces (e.g. plastered building walls that are common in central-European construction). The group of metals, found to have the most diverse radiative response in both the short- and long-wave region, is still under-represented in spectral libraries and requires special attention. Due to the development of new materials and coatings, the characterisation of the urban surface according to its spectral radiative response can expected to be an ongoing and dynamic process.

Impervious urban materials are complex because of their diverse compositions. Although a large number of samples have been analysed in the current study, more research is needed to understand the spectral response of the wide range of materials that comprise the urban surface. A comprehensive library covering the VIS–SWIR and the LWIR region for urban building materials could be the foundation for the development of a temperature–emissivity–separation (TES) algorithm applicable for the whole urban surface, including materials (e.g. metals) which pose problems for current TES methods (e.g. the ASTER TES algorithm; Sobrino et al., 2012). This would significantly advance urban remote sensing, and enhance the usability of thermal airborne or satellite imagery in these vitally important human environments.

Acknowledgements

This study was funded by (Grimmond) EUFP7 Grant agreement no. 211345 (BRIDGE), NERC ClearfLo (NE/H003231/1), the EPSRC (EP/I00159X/1, EP/I00159X/2) Materials Innovation Hub, and by King's College London. Martin Wooster's contribution was supported by the UK Natural Environment Research Council (NERC) National Centre for Earth Observation (NCEO). Much of the equipment was procured under the UK Science Research Investment Fund, or was loaned from the NERC Field Spectroscopy Facility (FSF). In addition to provision of equipment, we particularly thank Alasdair MacArthur and Chris MacLellan of NERC FSF for their detailed technical advice on the operation of both the SVC HR-1024 and the MIDAC FTIR and radiance calibration system. Some of the material samples were kindly provided by Paul Baldwin at ARUP. We thank Jeremy Bourdon and Margot Myers for their help in gathering material samples and Dr Bruce Main, Dr Trevor Blackall, Grace Healy, Oscar Finnemore, John Mustchin and Will Morrison for their assistance when performing certain of the measurements. Finally we thank Simon Hook at NASA JPL for providing the Ottawa sand sample.

Appendix A. Outdoor short-wave reflectance observations

In addition to the laboratory measurements, short-wave reflectance measurements were performed under outdoor conditions, too. These data are also included in the LUMA spectral library hence the methodology is outlined briefly.

The instrumental setup used for the outdoor measurements is the same as in the laboratory (Section 3.1.1), except that the sun was the source of irradiance instead of artificial light sources. Under clear sky conditions, diffuse radiation supplements the direct beam of sunlight so that irradiance conditions were in-between hemispherical (uniform irradiance from all directions over a hemisphere) and conical (irradiance restricted to a cone). As the incoming radiance travels through the atmosphere before interacting with the target and then the spectrometer effects of that path need to be considered. Field observations are thus generally restricted to clear sky conditions, when atmospheric effects (absorption or scattering of radiation by water vapour, gases and aerosols) are small. However, even under good weather conditions no useful surface spectral reflectance information can be easily obtained around the water vapour absorption lines (Peixoto and Oort, 1992), and thus spectra between 1350–1460 nm and 1790–1960 nm were removed from spectra collected in the field.

As in the lab, targets were sampled ten times. However, a different, random area of the target was moved into the FOV for every sample to better capture the heterogeneity of the materials. The panel was sampled after every fifth measurement to account for the potentially rapid variations in atmospheric conditions and their impact on the down-welling radiance. Unlike in the laboratory measurements, the SVC software was set to automatically merge the spectra at the overlap region of the silicon detector array and the first InGaAs detector.

Appendix B. Classes of impervious urban materials studied

Spectral response of materials grouped into ten classes is discussed in the current study (Section 4.2.1). Material characteristics and typical absorption/reststrahlen features are outlined here to provide the necessary context.

B.1. Quartzite conglomerate

Quartzite conglomerate coatings increase surface traction, and are applied to road surfaces in areas where traffic slow down is intended, such as pedestrian crossings (Paul Baldwin, ARUP, personal communication, June 2013). Geologically, quartzite originates from sandstone by heating or compression. The metamorphic rock is usually grey or white in colour, but depending on the minerals (e.g. iron oxide) in the composition it can also be yellow, red or pink. Quartzite is mainly composed of quartz and some feldspar. Both minerals show hardly any absorption features in the visible and near-infrared. However, they exhibit broad reflectance peaks between 8 and 10 μm (Lyon, 1964) caused by Si–O stretching vibrations. For quartz, an absorption peak divides these reststrahlen bands at 8.6 μm (Salisbury and D'Aria, 1992), thus forming a characteristic shape in the emissivity spectrum – the asymmetric quartz doublet. Maximum emissivity is reached at 7.4 and 12.2 μm, again caused by Si–O stretching vibration (Salisbury and D'Aria, 1992). Adjacent to the main doublet, a secondary, weaker one is formed between 12.3 and 13.0 μm.

B.2. Stone

Within the stone category are sedimentary rocks – sandstone and limestone. Both are used in crushed form as an ingredient for anthropogenic materials such as concrete, but are also often deployed for the construction of buildings or pavements directly. Limestone, composed mainly of calcium carbonate ($CaCO_3$), shows an absorption peak around 2350 nm caused by carbonate overtone vibrations (Hunt and Salisbury, 1971). Carbonate minerals (e.g. dolomite or calcite) exhibit further vibrational absorption bands at 1900 and 2550 nm (Gaffey, 1985). In the long-wave region, a reststrahlen band is located at around 11.3 μm (Christensen et al., 2000). As in quartzite, the primary constituents of sandstone are quartz and feldspar. Hence, it is the combination of minerals in the sandstone which give it its colour and are responsible for its spectral response in the VIS–SWIR (Bowen et al., 2007).

Iron oxides absorb in the region between 750 and 1300 nm (Bowen et al., 2007), with hematite giving a clear signature at 870 nm and goethite a broader absorption band around 930 nm (Deaton and Balsam, 1991). Clay minerals are usually connected to water absorption features at around 1400 and 1900 nm (Clark, 1999). For smectite minerals, the H_2O absorption at 1900 nm is generally stronger than for the kaolin or illite groups. Further,

hydroxyl combinations are responsible for absorption at 2200 nm, as a doublet in the case of kaolinite. Illite shows one feature at that band and further causes absorption at 2350 and 2450 nm (Bowen et al., 2007). Clay minerals are phyllosilicates (Deer et al., 1992) and so silica reststrahlen bands dominate the LWIR absorption of sandstone comprising those minerals.

B.3. Granite

Granite, one of the most abundant igneous rocks on the Earth's surface, is particularly hard, strong and quite resistant to weathering. Hence it is widely deployed as a construction material. It is used in buildings, roads and pavements, and is often favoured as street curbing material because it outperforms concrete in terms of resilience (Paul Baldwin, ARUP, personal communication June 2013). Mainly composed of quartz and feldspar, it is characterised by large grain sizes resulting in a colourful appearance, often as a combination of grey to white and red to pink shadings. In the short-wave region, granite can show H_2O vibration combinations at 1900 nm (Rivard et al., 1992).

B.4. Asphalt

Asphalt is the dominant material used for road surfaces in many European cities and worldwide, and is composed of a binder and some rocky aggregates of variable type and grain size. However, the minerals selected as aggregates vary with geological region and road type. Natural asphalt refers to the variety of natural bitumen (solid or semi-solid mixtures of hydrocarbons) that usually serves as binder in road construction materials (Meyer and de Witt, 1990). Although clearly dominated by a complex mixture of hydrogen and carbon constituents, most natural bitumen also contains nitrogen, oxygen, sulphur, and trace metals such as iron, nickel and vanadium (Meyer and de Witt, 1990).

Asphalt is a dark coloured material, typically black or grey. Broad absorption of hydrocarbon compounds are responsible for the overall low reflectance in the visible part of the spectrum, with no distinct absorption features due to the complex chemical structure of asphalt (Testa, 1995). A decrease in absorption with longer wavelengths is characteristic for hydrocarbons, such as in spectra of coals or oils (Cloutis, 1989). In the SWIR region where absorption is generally lower than in the VIS, two absorption features can often be identified: a C–H stretch first overtone band at 1730 nm and a C–H stretch combination band at 2310 nm (Cloutis, 1989).

The spectral reflectance of asphalt usually changes with age. It darkens due to tire abrasion and road cracking (Herold, 2007), while increased reflectance is observed after contamination with dust and abrasion of the asphaltic binder, the latter excavating larger fractions of the aggregate. Thus, older road surfaces may have mineral absorption features with weakened hydrocarbon signatures or the latter may be intensified from sealed cracks as bitumen patches are usually darker than asphalt itself because of the lack of aggregate.

Tarmac (short for tar-macadam) is a road surface material very close to asphalt. Macadam is the procedure used to combine aggregates with the tar binder, a hydrocarbon processed form of pitch. Other than the natural bitumen and asphalt, however, tar is made from wood or roots and is less close to crude oil. Still, the spectral radiative response of tarmac is similarly dominated by broad C–H absorption and hence included in the asphalt material class here.

B.5. Concrete and cement

Concrete, a ductile construction material of high strength, is deployed in a great variety of applications: construction of bridges and buildings (walls, roofs), roads and pavements (often as tiles). Concrete consists of cement with various aggregate materials of different grain sizes added. As aggregate usually makes up a large fraction of the concrete's volume it significantly determines the physical characteristics of the construction material, such as density and porosity. The most basic cement type combines ground clinker (calcium silicates) with a small percentage of gypsum (Mineral Product Association Cement, (MPA Cement, 2012)). Additional compounds such as fly ash (containing SiO_2 and CaO), limestone, or blast furnace slag (a combination of CaO, SiO_2, Al_2O_3, and MgO) may be added. The basic clinker is produced from natural minerals: calcium carbonate ($CaCO_3$) is decarbonized into calcium oxide (CaO) which then reacts with silica (SiO_2). Portland cement, one of the most common types, is composed of dicalcium silicate (Belite, Ca_2SiO_4) and tricalcium silicate (Alite, Ca_3SiO_5), which are responsible for the cements' strengths. Natural resources for calcium carbonate are in limestone, chalk and often other minerals (e.g. from clay and shale).

B.6. Brick

Bricks are commonly used in the construction of buildings (especially residential) and pavement in London and elsewhere. The *brick* category includes cuboids of rectangular plan and cross section made of original brick clay, but also those made of cement of various colours. Thus, the spectral features of cement block bricks are similar to the *concrete/cement* category.

Clay minerals evolve from silicate minerals by weathering. Hence, they can show characteristic absorption bands for water and hydroxyl ions. Other constituents of clay minerals include alumina, iron oxides, and carbonates. Absorption features of iron oxide at 520, 670, and 870 nm are clearly evident in VIS–SWIR spectra of new, red clay brick (Hunt, 1977; Ben-Dor et al., 2001; Herold et al., 2004). Brick clay is burned during the production process of *ceramic* materials, so that water and hydroxyl absorption features (typically found in spectra of fresh clay) are often diminished in the radiative response or might even be absent (Heiden et al., 2001). In the LWIR, clay minerals exhibit a broad absorption trough between about 8.5 and 10.5 μm. Absorption bands of common clay minerals include 9.8, 10.7, 12.6, and 14.5 μm (kaolinite), 9.6 μm (montmorillonite), and 9.7 μm (illite), and the wavelength of minimum absorption further varies with clay type (Hunt et al., 1950). Masonry has mortar as a binding material between the bricks/blocks composed of cement and sand, sometimes with lime or plasticizer added.

B.7. Roofing shingles and tiles

Shingles and tiles are both common roofing materials. They are distinguished here based on shape, with the shingles generally being "flat" rather than fabricated with a distinct shape (e.g. curved) to enhance prevention of rain entry into the building roof space. Roofing shingles sampled here are either natural slate or artificial fibre cement. Slate is a foliated metamorphic rock originated from shale, mainly composed of quartz and muscovite or illite. Even though slate naturally occurs in different colours, ranging from beige through purple to grey, dark grey or black shingles are installed most commonly. Slate is also applied as flooring (e.g. patios) or wall coverings. Fibre cement shingles are mainly used for roofing, but in some regions also for the cladding of walls. The material is composed of sand, cement and fibre (often cellulose).

Roofing tiles, commonly used for residential buildings in London, either consist of clay-based ceramics (and hence have similar features as clay bricks), or cement/concrete of different colours. As seen for clay bricks, the LWIR response of ceramic materials is characterised by a broad reststrahlen region with an absorption

Table C.1
Meta data for the London impervious urban materials samples, with their measured broadband albedo (300–2500 nm) and emissivity (8–14 μm).

ID	Class/Sub-class	Material	Colour	Status	Dimensions [mm]	Albedo	Emissivity
X001	Quartzite conglomerate	Quartzite	Beige/brown/black/red	New	360 × 4 × 220	0.26	0.92
X002	Quartzite conglomerate	Quartzite	Beige/brown/black/red	New	360 × 4 × 220	0.32	0.96
X003	Quartzite conglomerate	Quartzite	Brown	New	148 × 27 × 97	0.25	0.97
S001	Stone	Sandstone	Beige	Used	215 × 35 × 105	0.40	0.90
S002	Stone	Carboniferous coral limestone	Grey	Used	120 × 19 × 90	0.20	0.94
S003	Stone	Sandstone	Yellow	Used	120 × 80 × 27	0.26	0.93
S004	Stone	Limestone	Beige	Used	70 × 55 × 25	0.68	0.93
S005	Stone	Sandstone	Light grey	Smooth	28 × 75 × 180	0.46	0.92
G001	Granite	Granite	White/black	New, rough	142 × 56 × 52	0.48	0.92
G002	Granite	Granite with cement	White/red	Weathered	101 × 95 × 88	0.34	0.93
G003	Granite	Granite with cement	White/black	Weathered	215 × 57 × 105	0.41	0.89
G004	Granite	Granite	White/red/black	Weathered	233 × 60 × 78	0.54	0.93
G005	Granite	Granite	Red/black	Smooth	125 × 50 × 111	0.22	0.89
A001	Road asphalt	Asphalt with stone aggregate	Black/grey	Weathered	190 × 83 × 68	0.21	0.96
A002	Road asphalt	Asphalt with stone aggregate	Black/grey	Weathered	60 × 100 × 200	0.18	0.94
A003	Road asphalt	Asphalt with stone aggregate	Black/grey	Weathered	60 × 90 × 150	0.21	0.94
A004	Road asphalt	Asphalt with stone aggregate	Black/grey	Weathered	50 × 120 × 170	0.18	0.94
A005	Road asphalt	Asphalt with stone aggregate	Black/grey	Weathered	55 × 75 × 130	0.19	0.93
A006	Road asphalt	Asphalt with stone aggregate	Black/grey	Weathered	30 × 145 × 180	0.12	0.91
A007	Asphalt roofing shingle	Tarmac roofing paper	Grey	New	3 × 165 × 170	0.07	0.93
A008	Road asphalt	Tarmac	Black	Weathered	140 × 25 × 140	0.13	0.95
A009	Road asphalt	Tarmac	Black	Weathered	21 × 60 × 85	0.08	0.95
A010	Road asphalt	Tarmac	Black	Weathered	21 × 65 × 80	0.10	0.96
C001	Cement	Cement	Grey/ochre	Weathered	397 × 60 × 140	0.29	0.94
C002	Concrete	Concrete	Grey/white	New	198 × 53 × 100	0.21	0.92
C003	Cement	Cement	Grey	Weathered	268 × 44 × 148	0.23	0.91
C004	Concrete	Concrete	Grey	Weathered	110 × 72 × 85	0.37	0.95
C005	Cement	Cement	Grey	Weathered	45 × 80 × 115	0.41	0.95
C006	Concrete	Concrete	White	Weathered	90 × 150 × 250	0.42	0.95
C008	Concrete	Concrete	Grey	Weathered, rough	20 × 120 × 108	0.25	0.95
B001	Cement brick	Cement brick	Yellow	New	200 × 60 × 100	0.30	0.94
B002	Cement brick	Cement brick, with sand	Black/light grey	New	200 × 58 × 98	0.11	0.94
B003	Cement brick	Cement brick	Black	New	195 × 52 × 98	0.09	0.95
B004	Ceramic brick	Brick clay, with cement	Red	Weathered	62 × 35 × 52	0.31	0.91
B005	Cement brick	Cement brick	Red	Weathered	138 × 60 × 100	0.17	0.94
B006	Cement brick	Cement brick, with sand	Black	Weathered	200 × 60 × 100	0.20	0.89
B007	Cement brick	Cement brick	Light red	New	200 × 60 × 100	0.22	0.94
B008	Ceramic brick	Brick clay	Light red	New	63 × 100 × 212	0.43	0.94
B009	Cement brick	Cement	Red	Weathered, curvy	63 × 105 × 110	0.27	0.95
B010	Ceramic brick	Brick clay, painted	Red with beige and grey	Weathered	80 × 110 × 100	0.53	0.93
B011	Ceramic brick	Brick clay, with cement	Red/grey	Weathered	63 × 110 × 230	0.35	0.95
B012	Ceramic brick	Brick clay, painted	Red with white	Weathered, rough	70 × 112 × 107	0.56	0.95
B013	Ceramic brick	Brick clay	Red	Weathered	46 × 60 × 100	0.32	0.95
B014	Ceramic brick	Brick clay	Yellow/grey	Weathered, dusty	68 × 90 × 130	0.43	0.96
L001u	Roofing shingle	Slate	Black	Weathered	255 × 3 × 210	0.09	0.90
L001d	Roofing shingle	Slate	Black	Clear	255 × 3 × 210	0.14	0.93
L002	Roofing shingle	Fibre cement	Black	Weathered	232 × 3 × 241	0.05	0.94
L003	Roofing shingle	Fibre cement	Black	Weathered	230 × 207 × 3	0.06	0.95
R001	Ceramic roofing tile	Ceramic	Red	New	150 × 11 × 150	0.31	0.93
R002	Ceramic roofing tile	Ceramic	Brown	New	300 × 10 × 200	0.20	0.93
R003	Cement roofing tile	Cement	Rustic red	New	270 × 12 × 170	0.32	0.91
R004	Ceramic roofing tile	Ceramic	Burnt red	New	300 × 13 × 200	0.24	0.92
R005	Cement roofing tile	Cement	Rustic red with dark shading	New, shiny	260 × 12 × 165	0.17	0.96
R006	Cement roofing tile	Cement	Slate grey	New	265 × 11 × 165	0.12	0.94
R007	Ceramic roofing tile	Ceramic	Black	New	410 × 15 × 320	0.16	0.92
R008	Cement roofing tile	Cement	Rustic red	New, dull	260 × 12 × 165	0.26	0.95
R009	Cement roofing tile	Cement	Autumn red	New, rough	260 × 12 × 165	0.19	0.92
R010	Ceramic roofing tile	Ceramic	Red	Weathered	10 × 130 × 165	0.19	0.95
R012	Ceramic roofing tile	Ceramic	Red	Weathered	12 × 90 × 195	0.13	0.95
R013	Ceramic roofing tile	Ceramic	Red	Weathered	12 × 115 × 130	0.12	0.95
Z001	Metal	Aluminium plus zinc	Grey, dull	New	390 × 1 × 295	0.36	0.58
Z002	Metal	Aluminium, stucco	Grey, shiny	New	380 × 1 × 295	0.25	0.16
Z003	Metal painted	Metal with paint	Green	New	1 × 102 × 150	0.11	0.93
Z004	Metal painted	Metal with paint	Copper patina	New	1 × 150 × 192	0.45	0.94
Z005	Metal painted	Metal with paint	Slate grey	New	1 × 152 × 205	0.12	0.94
Z006	Metal	Aluminium	Grey	Weathered	1 × 220 × 230	0.26	0.81
Z007	Metal	Lead	Grey	Weathered	254 × 2 × 200	0.21	0.86
Z008	Metal	Iron	Black	Weathered	428 × 5 × 110	0.05	0.97
V001	PVC	PVC roofing material	Lead grey	New	1 × 146 × 204	0.08	0.94
V002	PVC	PVC roofing material	Light grey	New	1 × 146 × 204	0.43	0.93
V003	PVC	PVC roofing material	Copper brown	New, structured	1 × 146 × 204	0.29	0.94
V004	PVC	PVC roofing material	Azure blue	New	1 × 146 × 204	0.14	0.94
V005	PVC	PVC roofing material	Copper brown	New	1 × 146 × 204	0.17	0.94
V006	PVC	PVC roofing material	Copper patina	New	1 × 146 × 204	0.28	0.94

minimum around 9.3 μm, which, however, can shift significantly to longer or shorter wavelengths depending on the particular clay minerals involved. This signature is used here to subdivide the roofing tile category into ceramic tiles, and other roofing tiles – mostly made of cement/concrete.

B.8. Metals and PVC

Metals are quite often used as roofing materials (e.g. copper, aluminium), but also have other applications, especially in modern architecture. For example, the outer surfaces of modern skyscrapers are often largely composed of glass and metal. Common metals found in urban areas include steel, copper, aluminium and zinc (ZINC, 2003), often painted. Paint critically impacts the radiative response signatures, as these are generally determined by the upper 50 μm thick layer of the target (Ben-Dor et al., 2001). Thus, these coatings (Wray and Akbari, 2008) significantly alter the reflectance values. A similar effect is seen for the particular finishing (e.g. shiny or dull) used for the metal surfaces. Pure aluminium shows a broad and deep absorption band at 840 nm, while zinc has a similar feature at 1020 nm (Heiden et al., 2007). Absorption features of aluminium minerals (e.g. muscovite) can change their shape and position, depending on the aluminium in the crystal structure (Clark, 1999).

New roofing materials include sheets made of polyvinyl chloride (PVC). They can be manufactured in various colours and often are designed to resemble traditional roofing materials (e.g. copper or slate) in their optical appearance. Features dominated by hydrocarbon signatures include deep absorption at 1200, 1700 (caused by C–H stretch vibrations), 2170, and 2300 nm (Heiden et al., 2007; Cloutis, 1989). Pure colour pigments also have their effect.

Appendix C. Integrated broadband albedo and emissivity

The spectral response in the two regions of the electromagnetic spectrum can be integrated to broadband estimates. The latter are used in many modelling applications that commonly do not resolve the details of spectral variations, such as many land surface models. Given these integrated values are often applied in conjunction with broadband radiation estimates, the reflectance and emissivity spectra are weighted by appropriate reference spectra (Section 3.2) before performing the wavelengths aggregation.

Broadband estimates of short-wave albedo and long-wave emissivity were derived from the laboratory-based observations for all materials sampled (Table C.1). Overall, broadband values of the materials sampled have less variability in the LWIR ($0.89 > \varepsilon > 0.97$; only some metals with $0.16 < \varepsilon < 0.89$) than in the VIS–SWIR ($0.05 < \alpha < 0.68$). Materials dominated by hydrocarbons or quartz plus carbonates tend to have a higher emissivity compared to the other mineral classes. Quartz and ceramic materials constitute the most diverse groups with respect to their long-wave response. However, such trends are less evident for the short-wave albedo.

References

Abrams, M.J., Hook, S.J., 2013. NASA's hyperspectral infrared imager (HysplRI). In: Kuenzer, C., Dech, S. (Eds.), Thermal Infrared Remote Sensing. Springer, Netherlands, pp. 117–130.

Adam, E., Mutanga, O., Rugege, D., 2010. Multispectral and hyperspectral remote sensing for identification and mapping of wetland vegetation: a review. Wetl. Ecol. Manag. 18, 281–296.

Akbari, H., Menon, S., Rosenfeld, A., 2009. Global cooling: increasing world-wide urban albedos to offset CO2. Clim. Change 94, 275–286.

Baldridge, A.M., Hook, S.J., Grove, C.I., Rivera, G., 2009. The ASTER spectral library version 2.0. Remote Sens. Environ. 113, 711–715. http://dx.doi.org/10.1016/j.rse.2008.11.007.

Bassani, C., Cavalli, R.M., Cavalcante, F., Cuomo, V., Palombo, A., Pascucci, S., Pignatti, S., 2007. Deterioration status of asbestos-cement roofing sheets assessed by analyzing hyperspectral data. Remote Sens. Environ. 109, 361–378. http://dx.doi.org/10.1016/j.rse.2007.01.014.

Ben-Dor, E., Levin, N., Saaroni, H., 2001. A spectral based recognition of the urban environment using the visible and near-infrared spectral region (0.4-1.1 μm): a case study over Tel-Aviv, Israel. Int. J. Remote Sens. 22, 2193–2218. http://dx.doi.org/10.1080/01431160117759.

Borel, C.C., 1998. Surface emissivity and temperature retrieval for a hyperspectral sensor. IGARSS 98 Sensing and Managing the Environment, vol. 1. *IEEE Int. Geosci. Remote Sens. Symp.*, No98CH36174.

Bowen, B.B., Martini, B.A., Chan, M.A., Parry, W.T., 2007. Reflectance spectroscopic mapping of diagenetic heterogeneities and fluid-flow pathways in the Jurassic Navajo Sandstone. Am. Assoc. Pet. Geol. Bull. 91, 173–190. http://dx.doi.org/10.1306/08220605175.

Breen, C. et al., 2008. Bulk mineralogical characterisation of oilfield reservoir rocks and sandstones using diffuse reflectance infrared Fourier transform spectroscopy and partial least squares analysis. J. Pet. Sci. Eng. 60, 1–17, doi:10.1016/j.petrol.2007.05.001.

Brook, A., Ben-Dor, E., 2011. Reflectance spectroscopy as a tool to assess the quality of concrete in situ. J. Civ. Eng. Constr. Technol. 2, 168–188.

Cheng, J.C.J., Xiao, Q.X.Q., Li, X.L.X., Liu, Q.L.Q., Du, Y.D.Y., Nie, A.N.A., 2007. Evaluation of five algorithms for extracting soil emissivity from hyperspectral FTIR data. IEEE Int. Geosci. Remote Sens. Symp.. http://dx.doi.org/10.1109/IGARSS.2007.4423512.

Christensen, P.R., Bandfield, J.L., Hamilton, V.E., Howard, D.A., Lane, M.D., Piatek, J.L., Ruff, S.W., Stefanov, W.L., 2000. A thermal emission spectral library of rock-forming minerals. J. Geophys. Res. 105, 9735. http://dx.doi.org/10.1029/1998JE000624.

Clark, R.N., 1999. Spectroscopy of rocks and minerals, and principles of spectroscopy. In: Rencz, A.N. (Ed.), Manual of Remote Sensing, Remote Sensing for the Earth Sciences. John Wiley and Sons, New York, pp. 3–58.

Clark, R.N., Swayze, G.A., Wise, R., Livo, E., Hoefen, T., Kokaly, S.J., Sutley, R., 2007. USGS digital spectral library splib06a. U.S. Geol. Surv. Digit. Data Ser., 231, http://speclab.cr.usgs.gov/spectral.lib06/.

Cloutis, E.A., 1989. Spectral reflectance properties of hydrocarbons: remote-sensing implications. Science 245, 165–168. http://dx.doi.org/10.1126/science.245.4914.165.

Cloutis, E.A., Craig, M.A., Kruzelecky, R.V., Jamroz, W.R., Scott, A., Hawthorne, F.C., Mertzman, S.A., 2008. Spectral reflectance properties of minerals exposed to simulated Mars surface conditions. Icarus 195, 140–168. http://dx.doi.org/10.1016/j.icarus.2007.10.028.

Damtoft, J.S., Lukasik, J., Herfort, D., Sorrentino, D., Gartner, E.M., 2008. Sustainable development and climate change initiatives. Cem. Concr. Res. 38, 115–127.

Dash, A., Goettsche, F.-M., Olesen, F.-S., Fischer, H., 2002. Land surface temperature and emissivity estimation from passive sensor data: theory and practice-current trends. Int. J. Remote Sens. 23, 2563–2594.

DCLG, Department for Communities and Local Government, 2013. Next Steps to Zero Carbon Homes – Allowable Solutions, pp. 64. <https://www.gov.uk/government/consultations/next-steps-to-zero-carbon-homes-allowable-solutions> (accessed 08.04.14).

Deaton, B.C., Balsam, W.L., 1991. Visible spectroscopy – a rapid method for determining hematite and goethite concentration in geological materials. J. Sediment. Pet. 61 (4), 628–632.

Deer, W.A., Howie, R.A., Zussman, J., 1992. An Introduction to the Rock-Forming Minerals, second ed. Longman Scientific & Technical, pp. 528.

Deng, J.-S., Wang, K., Li, J., Deng, Y.-H., 2009. Urban land use change detection using multisensor satellite images. Pedosphere 19 (1), 96–103.

Franke, J., Roberts, D.A., Halligan, K., Menz, G., 2009. Hierarchical Multiple Endmember Spectral Mixture Analysis (MESMA) of hyperspectral imagery for urban environments. Remote Sens. Environ. 113, 1712–1723.

French, A.N., Schmugge, T.J., Ritchie, J.C., Hsu, A., Jacob, F., Ogawa, K., 2008. Detecting land cover change at the Jornada Experimental Range, New Mexico, with ASTER emissivities. Remote Sens. Environ. 112, 1730–1748.

Gaffey, S.J., 1985. Reflectance spectroscopy in the visible and near-infrared (0.35-2.55 μm): applications in carbonate petrology. Geology 13, 270–273. http://dx.doi.org/10.1130/0091-7613(1985) 13.

Gillespie, A., Rokugawa, S., Matsunaga, T., Cothern, J.S., Hook, S., Kahle, A.B., 1998. A temperature and emissivity separation algorithm for Advanced Spaceborne Thermal Emission and Reflection Radiometer (ASTER) images. IEEE T. Geosci. Remote 36, 1113–1126. http://dx.doi.org/10.1109/36.700995.

Griffiths, P.R., 1983. Fourier transform infrared spectrometry. Science 222, 297–302.

Hecker, C.A., Smith, T.E.L., da Luz, B.R., Wooster, M.J., 2013. Thermal infrared spectroscopy in the laboratory and field in support of land surface remote sensing. In: Kuenzer, C., Dech, S. (Eds.), Thermal Infrared Remote Sensing. Springer, Netherlands, pp. 43–67.

Heiden, U., Roessner, S., Segl, K., Kaufmann, H., 2001. Analysis of spectral signatures of urban surfaces for their identification using hyperspectral HyMap data. Remote Sensing and Data Fusion over Urban Areas, *IEEE/ISPRS Joint Workshop* 2001, pp. 173–177.

Heiden, U., Segl, K., Roessner, S., Kaufmann, H., 2007. Determination of robust spectral features for identification of urban surface materials in hyperspectral remote sensing data. Remote Sens. Environ. 111, 537–552.

Herold, M., 2007. Spectral characteristics of asphalt road surfaces. In: Weng, Q. (Ed.), Remote Sensing of Impervious Surfaces. CRC Press, Boca Raton, Florida, pp. 237–247.

Herold, M., Gardner, M., Roberts, D.A., 2003. Spectral resolution requirements for mapping urban areas. IEEE T. Geosci. Remote 41 (9), 1907–1919.

Herold, M., Roberts, D.A., Gardner, M.E., Dennison, P.E., 2004. Spectrometry for urban area remote sensing – development and analysis of a spectral library from 350 to 2400 nm. Remote Sens. Environ. 91, 304–319.

Hook, S.J., Kahle, A.B., 1996. The micro Fourier transform interferometer (μFTIR)—a new field spectrometer for acquisition of infrared data of natural surfaces. Remote Sens. Environ. 56, 172–181. http://dx.doi.org/10.1016/0034-4257(95)00231-6.

Hook, S.J., Johnson, W.R., Abrams, M.J., 2013. NASA's Hyperspectral Thermal Emission Spectrometer (HyTES). In: Kuenzer, C., Dech, S. (Eds.), Thermal Infrared Remote Sensing. Springer, Netherlands, pp. 93–115.

Horton, K.A., Johnson, J.R., Lucey, P.G., 1998. Infrared measurements of pristine and disturbed soils 2. Environmental effects and field data reduction. Remote Sens. Environ. 64, 47–52. http://dx.doi.org/10.1016/S0034-4257(97)00167-3.

Hunt, G.R., 1977. Spectral signatures of particulate minerals in the visible and near infrared. Geophysics 42, 501–513. http://dx.doi.org/10.1190/1.1440721.

Hunt, G.R., Salisbury, J.W., 1971. Visible and near infrared spectra of minerals and rocks II. Carbonates. Mod. Geol. 2, 23–30.

Hunt, J.M., Wisherd, M.P., Bonham, L.C., 1950. Infrared absorption spectra of minerals and other inorganic compounds. Anal. Chem. 22, 1478–1497.

Joseph, G., 2005. Fundamentals of Remote Sensing. Universities Press (India) Private Limited, pp. 486.

Kahle, A.B., Alley, R.E., 1992. Separation of temperature and emittance in remotely sensed radiance measurements. Remote Sens. Environ. 42, 107–111.

Kerekes, J.P., Strackerjan, K.-E., Salvaggio, C., 2008. Spectral reflectance and emissivity of man-made surfaces contaminated with environmental effects. Opt. Eng. 47, 106201.

King, T.V.V., Clark, R.N., 1989. Reflectance spectroscopy (0.2 to 20μm) as an analytical method for the detection of organics. In: Soils: Proceedings First International Symposium: Field Screening Methods for Hazardous Waste Site Investigations, EPA, pp. 485–488.

Korb, A.R., Dybwad, P., Wadsworth, W., Salisbury, J.W., 1996. Portable Fourier transform infrared spectroradiometer for field measurements of radiance and emissivity. Appl. Opt. 35, 1679–1692. http://dx.doi.org/10.1364/AO.35.001679.

Kotthaus, S., 2014. Implications of the Dense City Centre to Surface-Atmosphere Exchanges. King's College London, PhD Thesis, pp. 292.

Kuenzer, C., Dech, S., 2013. Thermal Infrared Remote Sensing: Sensors, Methods, Applications. Springer, pp. 544.

Kusaka, H., Kondo, H., Kikegawa, Y., Kimura, F., 2001. A simple single-layer urban canopy model for atmospheric models: comparison with multi-layer and slab models. Bound. Lay. Met. 101, 329–358.

Lindermeir, E., Haschberger, P., Tank, V., Dietl, H., 1992. Calibration of a Fourier transform spectrometer using three blackbody sources. Appl. Opt. 31, 4527. http://dx.doi.org/10.1364/AO.31.004527.

Lyon, R.J.P., 1964. Evaluation of infrared spectrophotometry for compositional analysis of lunar and planetary soils. Part II: Rough and Powdered Surfaces: NASA Contractor, Report CR-100, 262 pp.

Matzarakis, A., Rutz, F., Mayer, H., 2010. Modelling radiation fluxes in simple and complex environments: basics of the RayMan model. Int. J. Biometeorol. 54, 131–139.

Meyer, R.F., de Witt, W., 1990. Definition and world resources of natural bitumens. *U.S.* Geol. Surv. Bull. 1944, 1–14.

MPA Cement, 2012. Mineral Products Association (MPA) Cement. <http://cement.mineralproducts.org/cement/manufacture/types_of_cement.php> (accessed 10.07.13).

Nasarudin, N.E.M., Shafri, H.Z.M., 2011. Development and Utilization of Urban Spectral Library for Remote Sensing of Urban Environment. J. Urban. Env. Eng. 5 (1), 44–56.

NREL, 2000. The National Renewable Energy Laboratory, ASTM G173-03. <http://rredc.nrel.gov/solar/spectra/am1.5/#about> (accessed 27.05.13).

Ottle, C., Stoll, M., 1993. Effect of atmospheric absorption and surface emissivity on the determination of land surface temperature from infrared satellite data. Int. J. Remote Sens. 14, 2025–2037.

Pascucci, S., Bassani, C., Palombo, A., Poscolieri, M., Cavalli, R., 2008. Road asphalt pavements analyzed by airborne thermal remote sensing: preliminary results of the Venice highway. Sensors 8, 1278–1296. http://dx.doi.org/10.3390/s8021278.

Peixoto, J.P., Oort, A.H., 1992. Physics of Climate. American Institute of Physics, pp. 520.

Peres, L.F., Sobrino, J.A., Libonati, R., Jiménez-Muñoz, J.C., Dacamara, C.C., Romaguera, M., 2008. Validation of a temperature emissivity separation hybrid method from airborne hyperspectral scanner data and ground measurements in the SEN2FLEX field campaign. Int. J. Remote Sens. 29, 7251–7268.

Planck, M., 1901. Ueber das Gesetz der Energieverteilung im Normalspectrum. Ann. Phys. 309, 553–563. http://dx.doi.org/10.1002/andp.19013090310.

Price, J.C., 1995. Examples of high resolution visible to near-infrared reflectance spectra and a standardized collection for remote sensing studies. Int. J. Remote Sens. 16, 993–1000. http://dx.doi.org/10.1080/01431169508954459.

R Core Team, 2005. R: A Language and Environment for Statistical Computing. R Foundation for Statistical Computing, Vienna, Austria. <http://www.R-Project.org/>.

Revercomb, H.E., Buijs, H., Howell, H.B., Laporte, D.D., Smith, W.L., Sromovsky, L.A., 1988. Radiometric calibration of IR Fourier transform spectrometers – solution to a problem with the high-resolution interferometer sounder. Appl. Opt. 27, 3210–3218.

Rivard, B., Arvidson, R.E., Duncan, I.J., Sultan, M., Elkaliouby, B., 1992. Varnish, sediment, and rock controls on spectral reflectance of outcrops in arid regions. Geology 20, 295–298. http://dx.doi.org/10.1130/0091-7613(1992) 020<0295:vsarco>2.3.co;2.

Roberts, D.A., Quattrochi, D.A., Hulley, G.C., Hook, S.J., Green, R.O., 2012. Synergies between VSWIR and TIR data for the urban environment: an evaluation of the potential for the Hyperspectral Infrared Imager (HysplRI) Decadal Survey mission. Remote Sens. Environ. 117, 83–101. http://dx.doi.org/10.1016/j.rse.2011.07.021.

Robinson, I., Mac Arthur, A., 2012. The FSF Post Processing Toolbox User Guide: Post Processing Spectral Data in MATLAB, 1–26.

Rodriguez, M.A., Liso, M.J., Rubio, F., Rubio, J., Oteo, J.L., 1999. Study of the reaction of γ-methacryloxypropyltrimethoxysilane (γ-MPS) with slate surfaces. J. Mater. Sci. 34, 3867–3873. http://dx.doi.org/10.1023/A:1004666621479.

Roessner, S., Segl, K., Heiden, U., Kaufmann, H., 2001. Automated differentiation of urban surfaces based on airborne hyperspectral imagery. IEEE T. Geosci. Remote 39, 1525–1532.

Rossel, R.A.V., McGlynn, R.N., McBratney, A.B., 2006. Determining the composition of mineral-organic mixes using UV - vis - NIR diffuse reflectance spectroscopy. Geoderma 137, 70–82. http://dx.doi.org/10.1016/j.geoderma.2006.07.004.

Ruff, S.W., Christensen, P.R., Barbera, P.W., Anderson, D.L., 1997. Quantitative thermal emission spectroscopy of minerals: a laboratory technique for measurement and calibration. J. Geophys. Res. 102, 14899–14913. http://dx.doi.org/10.1029/97JB00593.

Salisbury, J.W., D'Aria, D.M., 1992. Emissivity of terrestrial materials in the 8–14 μm atmospheric window. Remote Sens. Environ. 42, 83–106. http://dx.doi.org/10.1016/0034-4257(92)90092-X.

Salvaggio, C., Miller, C.J., 2001. Methodologies and protocols for the collection of midwave and longwave infrared emissivity spectra using a portable field spectrometer. In: Proceedings of the SPIE, SPIE AeroSense, Image Exploitation and Target Recognition, Algorithms and Technologies for Multispectral, Hyperspectral, and Ultraspectral Imagery VII, vol. 4381. Orlando, Florida, USA, 539–548.

Savitzky, A., Golay, M.J.E., 1964. Smoothing and differentiation of data by simplified least squares procedures. Anal. Chem. 36, 1627–1639. http://dx.doi.org/10.1021/ac60214a047.

Schueler, T.R., 1994. The importance of imperviousnes. Watershed Prot. Tech. 1 (3), 100–111.

Small, C., 2006. Comparative analysis of urban reflectance and surface temperature. Remote Sens. Environ. 104 (2), 168–189.

Sobrino, J.A., Oltra-Carrió, R., Jiménez-Muñoz, J.C., Julien, Y., Sòria, G., Franch, B., Mattar, C., 2012. Emissivity mapping over urban areas using a classification-based approach: application to the Dual-use European Security IR Experiment (DESIREX). Int. J. Appl. Earth Obs. Geoinf. 18, 141–147. http://dx.doi.org/10.1016/j.jag.2012.01.022.

Testa, S.M., 1995. Chemical aspects of cold-mix asphalt incorporating contaminated soil. J. Soil Contam. 4.

The Guardian, 2013. Walkie Talkie architect 'didn't realise it was going to be so hot'. Available at: <http://www.theguardian.com/artanddesign/2013/sep/06/walkie-talkie-architect-predicted-reflection-sun-rays>. (accessed 10.01.14).

Tomlinson, C.J., Chapman, L., Thornes, J.E., Baker, C., 2011. Remote sensing land surface temperature for meteorology and climatology: a review. Meteorol. Appl. 18, 296–306.

Townshend, J., Justice, C., Li, W., Gurney, C., McManus, J., 1991. Global land cover classification by remote sensing: present capabilities and future possibilities. Remote Sens. Environ. 35, 243–255. http://dx.doi.org/10.1016/0034-4257(91)90016-Y.

Van der Meer, F.D., Jong, S.M., 2002. Imaging Spectrometry: Basic Principles and Prospective Applications. Kluwer Academic, pp. 425.

Voogt, J.A., Grimmond, C.S.B., 2000. Modeling surface sensible heat flux using surface radiative temperatures in a simple urban area. J. Appl. Meteorol. 1681, 1669–1679.

Voogt, J.A., Oke, T.R., 2003. Thermal remote sensing of urban climates. Remote Sens. Environ. 86, 370–384.

Wan, Z., Ng, D., Dozier, J., 1994. Spectral emissivity measurements of land-surface materials and related radiative transfer simulations. Adv. Sp. Res. 14, 91–94. http://dx.doi.org/10.1016/0273-1177(94)90197-X.

Weng, Q., 2012. Remote sensing of impervious surfaces in the urban areas: requirements, methods, and trends. Remote Sens. Environ. 117, 34–49. http://dx.doi.org/10.1016/j.rse.2011.02.030.

Wooster, M.J. et al., 2011. Field determination of biomass burning emission ratios and factors via open-path FTIR spectroscopy and fire radiative power assessment: headfire, backfire and residual smouldering combustion in African savannahs. Atmos. Chem. Phys. 11, 11591–11615, doi:10.5194/acp-11-11591-2011..

Wray, C., Akbari, H., 2008. The effects of roof reflectance on air temperatures surrounding a rooftop condensing unit. Energ. Build. 40, 11–28.

Xu, W., Wooster, M.J., Grimmond, C.S.B., 2008. Modelling of urban sensible heat flux at multiple spatial scales: a demonstration using airborne hyperspectral imagery of Shanghai and a temperature-emissivity separation approach. Remote Sens. Environ. 112, 3493–3510. http://dx.doi.org/10.1016/j.rse.2008.04.009.

Yaghoobian, N., Kleissl, J., 2012. Effect of reflective pavements on building energy use. Urban Clim. 2, 25–42. http://dx.doi.org/10.1016/j.uclim.2012.09.002.

Yang, X., 2011. Urban Remote Sensing: Monitoring, Synthesis and Modeling in the Urban Environment. Wiley-Blackwell, Chichester, UK, pp. 388.

ZINC, 2003. Zinc Applications. Zinc Info Centre. <http://www.zincinfocentre.org/zinc_applications.html> (accessed 27.11.13).